Available online at www.sciencedirect.com
SCIENCE DIRECT®
Coordination Chemistry Reviews 249 (2005) 1870–1901
COORDINATION CHEMISTRY REVIEWS
www.elsevier.com/locate/ccr

Review

Gold nanorods: Synthesis, characterization and applications

Jorge Pérez-Juste [a,*], Isabel Pastoriza-Santos [a], Luis M. Liz-Marzán [a], Paul Mulvaney [b]

[a] *Departamento de Química Física, Universidade de Vigo, 36310 Vigo, Spain*
[b] *Chemistry School, University of Melbourne, Parkville, VIC 3010, Australia*

Received 3 November 2004; accepted 27 January 2005
Available online 1 April 2005

Contents

Abstract

This article provides an overview of current research into the synthesis and properties of gold nanorods. Interest in rod-shaped nanoparticles stems from their unique optical properties, which can be approximated by Mie–Gans theory. We begin by outlining briefly the origin of the

* Corresponding author. Tel.: +34 986 812307; fax: +34 986 812556.
E-mail address: juste@uvigo.es (J. Pérez-Juste).

0010-8545/$ – see front matter
doi:10.1016/j.ccr.2005.01.030

shape-dependent optical properties of rods. The different synthetic strategies that have been developed to achieve decent yields and sample monodispersity are then described, and the methods used for physical characterization as well as results of inorganic structure studies follow. Some of the most innovative research dealing with surface modification and chemical reactivity of gold nanorods is highlighted, together with new directions such as the synthesis of core-shell particles and the interactions of gold nanorods with biomolecules. Gold nanorods can be excited by ultrafast laser-induced heating; the resulting relaxation processes are important in determining the material properties of the metal particles. In addition, vibrational modes and shape changes are elucidated, and a theoretical analysis of the expected behavior is also presented. The incorporation of the gold nanorods into thin films and gels provides a new avenue for designing and growing materials with anisotropic optical properties. Initial results on the optical properties of such nanocomposites are reviewed. This review is concluded with a section devoted to the future perspectives for gold rods as novel materials.

Keywords: Gold nanorods; Mie–Gans theory; Laser-induced heating; Nanoparticle synthesis; Nanocomposites

1. Introduction

Nanoscience is the exploration of materials on nanometer lengthscales. The wet-chemical synthesis of such novel materials is a field at the crossroads of conventional inorganic cluster chemistry and classical colloid chemistry. These new materials will lay the foundations for a whole set of technological developments which are commonly termed nanotechnology, and that have in common the use and manipulation of objects with at least one dimension in the nanometer size range (typically 1–100 nm). Although quite a few approaches have been developed for the creation of such objects, wet chemistry promises to become the preferred choice, because of its relative simplicity and use of inexpensive materials. The aim of such synthesis is generally the preparation of various kinds of nanoparticles of controlled composition, shape and size, so that the influence of particle radius on the physical, chemical, optical, electronic and catalytic properties of the material can be studied and correlated with modern quantum theory. To date the most widely studied nanoparticles have been those made of metals, semiconductors and magnetic materials. Once size control and monodispersity have been reasonably achieved, the next level of sophistication is shape control, i.e., synthesis of non-spherical nanoparticles where not only the size, but also other topological aspects can be controlled through judicious choice of experimental conditions and additives. For example, materials may be fashioned as rods, tubes or concentric core-shell structures, as hollow capsules or alloys. To move beyond conventional spherical growth, additives are used which bind to the nanoparticle surface. Such "coordination chemistry" between surfactants, ligands, adsorbates, passivants, chelating agents or polymers and nanoparticle surface atoms is of fundamental importance in achieving shape control. To date, the specific mechanisms governing morphology and geometry control over particle growth are still far from being well understood, this is expected to stimulate considerable the research over the next decade. It is immediately apparent that such basic studies of crystal morphology will lead to models for the more complex processes involved in biomaterial synthesis and the development of sophisticated skeletal architecture in living systems.

This review will focus on the latest advances in the chemical synthesis of metal nanorods, in particular of gold nanorods, as well as their properties and some applications. These particles are primarily interesting from the point of view of their optical properties, which strongly depend on both the particle size and shape. Such optical properties are related to the interaction between the metal conduction electrons and the electric field component of incident electromagnetic radiation, which in the case of a few metals, such as gold and silver, leads to strong, characteristic absorption bands in the visible part of the spectrum, and in turn to unusual bright colors, not observed in the bulk material. The basic elements of the theory behind this phenomenon are described in Section 2, since the optical spectrum is directly correlated to the aspect ratio of the particles. Consequently, the formation of nanorods in solution can be easily monitored using standard UV–vis–NIR spectroscopy, which enables the mechanism behind the growth of these particles along a preferred orientation to be investigated. The current synthetic methods are then thoroughly described, including a review of the structural characterization that has been performed on them. Section 5 describes experiments on surface modification of gold nanorods, as well as the influence of surface-active compounds on the rod properties, while Section 6 focuses on ultrafast optical studies of the mechanical properties of nanorods and the physical effects of irradiation with intense laser beams. Section 7 summarizes the few reports available on the incorporation of gold nanorods within solid matrices to form nanocomposites, and finally, Section 8 briefly describes some applications for these materials.

2. Optical properties of metal nanorods

In this section, we review some of the key attributes of non-spherical particles. An understanding of the basic optical properties is important for several distinct reasons. On the one hand, small particles may have electronic, crystallographic, mechanical or catalytic properties that are different to the bulk material. Such differences may be probed through op-

tical measurements. Secondly, spectroscopic measurements are often the easiest methods for monitoring surface processes such as dissolution and precipitation, adsorption and electron transfer. For example, there is currently strong interest in pushing analytical chemistry towards single molecule detection and identification. This could be feasible using surface enhanced Raman spectroscopy of molecules on anisotropic metal surfaces, and various geometries for achieving this have been proposed. Furthermore, there is growing recognition of the opportunity to build nanoscale designer materials using "bottom-up" assembly. If nanocrystals of any specific geometry could be grown then it is conceivable that optical materials could be designed from scratch. Photonic devices could be created from molecular growth reactors.

This particular section is intended only to provide the foundation for interpreting experimental data included in Sections 3–7. Comprehensive reviews of the optical properties of metal particles are given in a range of texts and journals that discuss electromagnetic theory, size effects [1–3], the light scattering features or the surface chemical perturbations [4]. Textbooks giving thorough treatments include those by van der Hulst [5], Kerker [6] and Bohren and Huffman [7]. More recent work has involved the development of robust numerical solutions to the light scattering and extinction by non-spherical structures including 2D arrays [8]. The review by Kelly et al. provides an excellent overview [9], while computational aspects are covered by several authors [10–12].

2.1. Absorption by small metal spheres

We are concerned with solutions containing small nanocrystals. These particles do not sediment and the solution is optically and spatially homogeneous. In a dilute colloidal solution containing N particles per unit volume, the measured attenuation of light of intensity I_0, over a path length x cm in a spectrophotometer is given in differential form as:

$$\frac{\mathrm{d}I(x)}{\mathrm{d}x} = -NC_{\mathrm{ext}}I(x) \tag{2.1}$$

which shows that the rate of loss of photons is proportional to the light intensity at distance x into the medium, and also to the number density of light extinguishing particles. Integration gives the solution absorbance:

$$A = \log_{10}\frac{I_0}{I(x)} = \frac{NC_{\mathrm{ext}}x}{2.303} \tag{2.2}$$

where C_{ext} is the extinction cross-section of a single particle. For spherical particles with a wavelength-dependent dielectric function $\varepsilon(\lambda) = \varepsilon'(\lambda) + i\varepsilon''(\lambda)$, embedded in a medium of dielectric function ε_{m}, C_{ext} is given by [5–7]:

$$C_{\mathrm{ext}} = \frac{2\pi}{k^2}\sum_{n=1}^{n=\infty}(2n+1)Re\{a_n + b_n\} \tag{2.3}$$

where

$$k = 2\pi\frac{\sqrt{\varepsilon_{\mathrm{m}}}}{\lambda}, \tag{2.4}$$

and a_n and b_n are the scattering coefficients, which are functions of the particle radius and λ in terms of Ricatti–Bessel functions. The extinction cross-section of a particle is often normalized to give the extinction cross-section per unit area:

$$Q_{\mathrm{ext}} = \frac{C_{\mathrm{ext}}}{\pi R^2} \tag{2.5}$$

Conventionally, chemists measure the extinction coefficient of a solution in units of $\mathrm{M}^{-1}\,\mathrm{cm}^{-1}$, where the concentration is the molar metal atom concentration. For particles of radius R (cm), this quantity is related to Q_{ext} by:

$$\varepsilon(\mathrm{M}^{-1}\mathrm{cm}^{-1}) = \frac{3\times 10^{-3}V_{\mathrm{m}}Q_{\mathrm{ext}}}{(4\times 2.303R)} \tag{2.6}$$

where V_{m} ($\mathrm{cm}^3\,\mathrm{mol}^{-1}$) is the molar volume of the metal. Bohren and Huffman provide various approximations that may be used instead of the full series expansion [7]. In particular, for very small particles where $kR \ll 1$, only the first few terms are important in these equations.

$$a_1 = -\frac{i2x^3}{3}\frac{m^2-1}{m^2+2} - \frac{i2x^5}{5}\frac{(m^2-2)(m^2-1)}{(m^2+2)^2} + \frac{i4x^6}{9}\left[\frac{m^2-1}{m^2+2}\right]^2 + O(x^7) \tag{2.7}$$

$$a_2 = -\frac{i2x^5}{15}\frac{m^2-1}{2m^2+2} + O(x^7) \tag{2.8}$$

$$b_1 = -\frac{ix^5}{45}(m^2-1) + O(x^7) \tag{2.9}$$

$$b_2 = O(x^7) \tag{2.10}$$

Here m is the refractive index of the material relative to the medium, i.e., $m = n/n_{\mathrm{med}}$ and $x = kR = 2\pi n_{\mathrm{med}}R/\lambda$. If we retain just the first term in a_1, then Eq. (2.3) becomes:

$$C_{\mathrm{ext}} = \frac{24\pi^2R^3\varepsilon_{\mathrm{m}}^{3/2}}{\lambda}\frac{\varepsilon''}{(\varepsilon'+2\varepsilon_{\mathrm{m}})^2+\varepsilon''^2} \tag{2.11}$$

This equation can also be obtained by purely electrostatic arguments, and a succinct derivation is given elsewhere [13]. Note that C_{ext} scales as R^3, while the number density decreases as R^3 for a given amount of colloidal material. Hence, the molar absorption coefficient is independent of particle size. This is borne out for particles in the range up to about 30 nm, where scattering begins to be significant. For very small particles, <5–10 nm in diameter, the material properties themselves change, and this results in changes to the dielectric function, $\varepsilon(\lambda)$, and hence to the colloid optical properties. A curious feature of Eq. (2.11) is that there is no absorption if $\varepsilon'' = 0$ but there is also no absorption if $\varepsilon'' = \infty$. In the first

case, the particle is simply non-absorbing, while in the second case, it reflects all incident radiation.

Mie was able to explain some of the anomalous and striking colors exhibited by small metal particles, particularly those of gold or silver [14]. In these measurements, it is assumed that the refractive index and absorption coefficient of the dispersed particles are known. These are usually gleaned from reflection measurements on pure thin films in vacuum [15].

The reason that metals exhibit such strong optical effects is due to the dynamic response of the electrons. The dielectric function is related to the complex refractive index, n, through $\varepsilon(\lambda) = (n + ik)^2$. For metals, the dielectric function typically takes the form:

$$\varepsilon'(\lambda) = \varepsilon(0) - \frac{\lambda^2}{\lambda_p^2} \tag{2.12a}$$

$$\varepsilon''(\lambda) = \frac{\lambda(\lambda^2 + \lambda_d^2)}{\lambda_p^2 \lambda_d} \tag{2.12b}$$

The first term in Eq. (2.12a) is the short wavelength dielectric constant, which subsumes all UV absorption bands.

$$\lambda_p = \frac{2\pi c}{\omega_p} = \sqrt{\frac{4\pi^2 c^2 m \varepsilon_o}{Ne^2}} \tag{2.13}$$

The plasma wavelength, λ_p, is characteristic for each metal, and is a function of only the electron density, N, and the effective mass of electrons, m, in the material. λ_d is the damping constant of the conduction electrons. Surface plasmon absorption due to the confined excitation of conduction electrons in small particles occurs because the dielectric function $\varepsilon(\lambda)$ can take negative values, leading to poles in the value of a_1. The position of the surface plasmon absorption band of small gold spheres is given to a good approximation by the condition:

$$\varepsilon_1 = -2\varepsilon_m. \tag{2.14}$$

Here, $\varepsilon_m = n_{med}^2$ is the dielectric function of the (non-absorbing) solvent, and ε_1 is the real part of the dielectric function of the metal at that energy or wavelength. Previous work suggests that the dielectric data obtained from reflectivity measurements on bulk metal may be in error by about 1–3%. Such small errors are inevitable from the Kramers–Kronig analysis, but the predicted surface plasmon band position may consequently be in error by up to 10 nm.

2.2. Absorption by small metal ellipsoids

In 1912, Gans predicted [16] that for very small ellipsoids, where the dipole approximation holds, the surface plasmon mode would split into two distinct modes. This is a consequence of the surface curvature, which determines classically the restoring force or depolarization field that acts on the confined conduction electron population. He quantified the response as a function of the ellipsoid aspect ratio. As will be seen later, electron microscopy reveals that most nanorods are more like cylinders or sphero-capped cylinders than ellipsoids. However, an analytical solution for such shapes is not possible. Solutions have been found for the case of an infinite cylinder and for oblate and prolate ellipsoids. Ruppin has published a number of studies into light scattering by finite dielectric cylinders [17,18], while Fuchs has provided numerical solutions for the modes of a cube-shaped nanocrystal [19]. In the same article, he provides a method for numerical solution to the general problem of modes in non-spherical particles via a surface integral technique, which appears to be an alternative to the discrete dipole approximation (DDA) approach. Numerical methods, especially the T-matrix [20,21] and DDA technique [11,22,23] have been applied to small particles. Schatz and co-workers have recently reviewed this approach [9].

Because of the difficulty in preparing non-spherical samples, little experimental work to support Gans formulation existed until the 1950s. In the 1960s, Stookey and Araujo [24] stretched glasses containing small silver spheres. The small particles were aligned in the molten glass to form necklaces, which exhibited red-shifted absorption spectra. Other work involved thermally evaporating silver or gold through angled masks to create small, anisotropic, 2D layers of metal on glass substrates. More recently, it has become possible to chemically prepare small gold rods (see Section 3). In explaining the optical properties of these small rods, it has been common to treat them as ellipsoids [25–28], which allows the Gans formula to be applied. The polarizability of an ellipsoid is given by:

$$\alpha_{x,y,z} = \frac{4\pi abc(\varepsilon_{Au} - \varepsilon_m)}{3\varepsilon_m + 3L_{x,y,z}(\varepsilon_{Au} - \varepsilon_m)} \tag{2.15}$$

Here a, b and c refer to the length of the ellipse along the x, y and z axes ($a > b = c$), ε_{Au} the dielectric function of Au, ε_m the dielectric constant of the medium at optical frequencies and $L_{x,y,z}$ is the depolarization factor for the respective axis, which is given by:

$$L_x = \frac{1 - e^2}{e^2}\left(-1 + \frac{1}{2e}\ln\frac{1+e}{1-e}\right);$$

$$L_{y,z} = \frac{(1 - L_x)}{2} \tag{2.16}$$

Here, e is the rod ellipticity given by $e^2 = 1 - (b/a)^2$. For a sphere $e = 0$ and $L = 1/3$. The polarizability is related directly to the extinction of light by $C_{ext} = kI(\alpha)$ (Fig. 2.1).

These equations provide the stimulation for much of the subsequent experimental work on the growth and synthesis of gold and metal rods. The implication is clear. If the material growth parameters can be controlled, materials with tunable absorption spectra can be synthesized. Given that metals are generally photostable, unlike semiconductors, there should be many applications for such materials in optics, thin films and coatings. Oriented ellipsoids and cylinders should exhibit strong, polarization-dependent optical spectra. Finally,

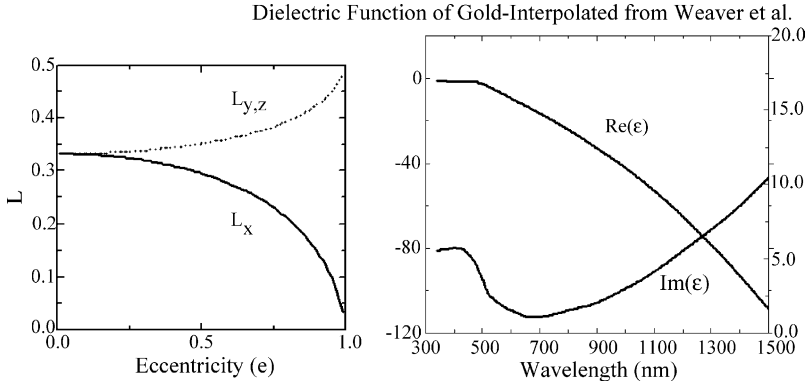

Fig. 2.1. Depolarization of a prolate spheroid vs. eccentricity, *e*, along the major axis, *x* and the two equivalent minor axes, *y* and *z* (left). The real and imaginary parts of the dielectric function of bulk gold (right).

the successful chemical growth of small rods and cylinders may signal the advent of systematic fabrication of nanowires and even electronic circuitry through wet-chemical processing.

2.3. The effect of aspect ratio

Gans' equation predicts how the plasmon mode peak position varies with aspect ratio for small ellipsoids embedded in the same medium. The easiest way to visualize this is to plot the depolarization factor *L* in Eq. (2.16) versus the value of the dielectric function at the peak (Fig. 2.2).

A common observation from combining electron microscopy sizing of Au nanocrystals with spectral measurements is an almost linear correlation between peak position and aspect ratio. Results from Pérez-Juste et al. [29] are shown in Fig. 2.3.

Small changes in aspect ratio lead to drastic changes in transmitted colors as seen in the samples in Fig. 2.4. The fact that the plasmon band appears to be drastically red-shifted from the positions predicted by the Gans model, yet still displays the linearity expected from Eqs. (2.15) and (2.16), led El-Sayed and co-workers to propose [27] that the water layers around the rods were polarized and had a substantially higher refractive index than water. Yan et al. [30] pointed out that their analysis contains a mathematical flaw; yet even so it is clear that the discrepancy needs to be explained. From the micrographs shown below, one explanation is that cylindrical particles exhibit surface plasmon longitudinal (SP_{long}) bands red-shifted from those of similar sized ellipsoids.

2.4. The effect of the refractive index of the solvent

Gold nanorods change color when embedded in different solvents of varying refractive index. Typical experimental data are shown in the left hand graph of Fig. 2.5, while the right hand graph shows a plot of the peak position versus solvent refractive index. Note that the peak absorption and the peak width both increase as *n* increases.

Calculated spectra for ellipsoids in different media are shown in Fig. 2.6. As can be seen the shifts are quite dramatic. The gold nanorods are extremely sensitive to the dielectric properties of their environment. The calculations predict stronger shifts than are observed experimentally. The

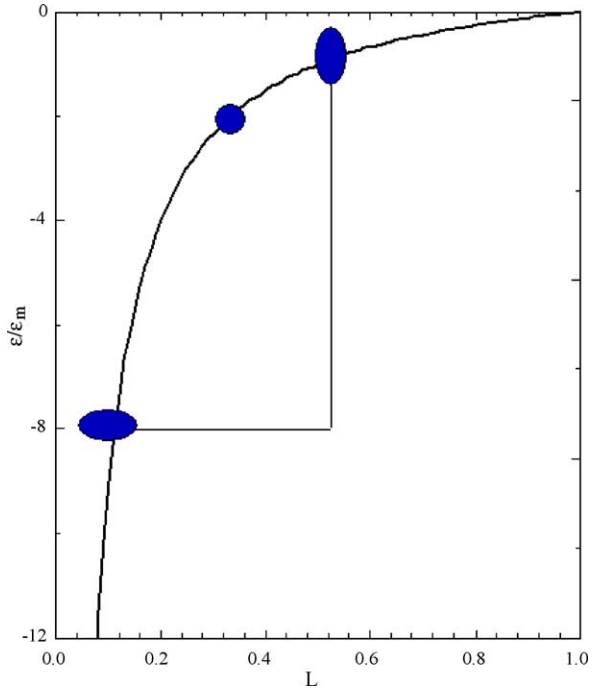

Fig. 2.2. The ratio of the dielectric function of the material to the medium for different polarization factors. For a sphere, the single plasmon mode occurs at $\varepsilon/\varepsilon_m = -2$, corresponding to $L = 1/3$. When the degeneracy is lifted, two modes split out from this point. The transverse mode asymptotes towards $L = 1.0$, giving a peak at the wavelength where the dielectric function of the metal is zero. This is the condition for surface plasmon excitation of an infinite surface slab. For Au, this is about 510 nm in water (as compared to 520 nm for spheres) so the transverse band blue shifts only slightly as the rods grow. Conversely, the longitudinal mode continues to slide to more negative values of $\varepsilon/\varepsilon_m$, corresponding to longer wavelengths, according to Eq. (2.16).

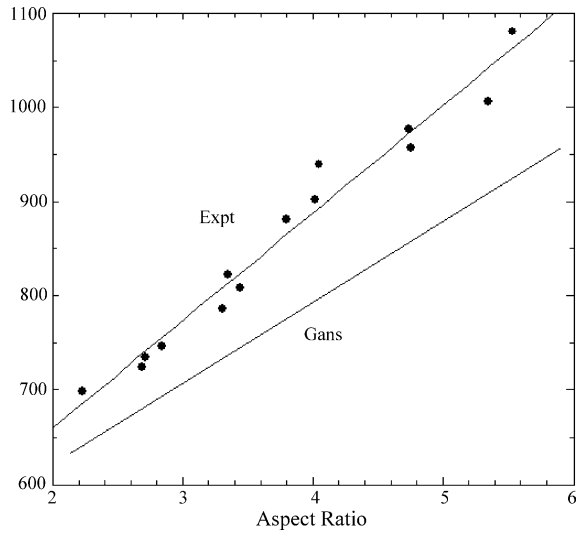

Fig. 2.3. Experimental plot of the surface plasmon longitudinal band position vs. aspect ratio for pure gold rods in water. This linear correlation is fortuitous. Over large aspect ratio values, the Gans formula predicts a slow curvature. Furthermore, retardation effects and radiation damping become more prominent for larger aspect ratios. These effects are not included in the basic ellipsoid model.

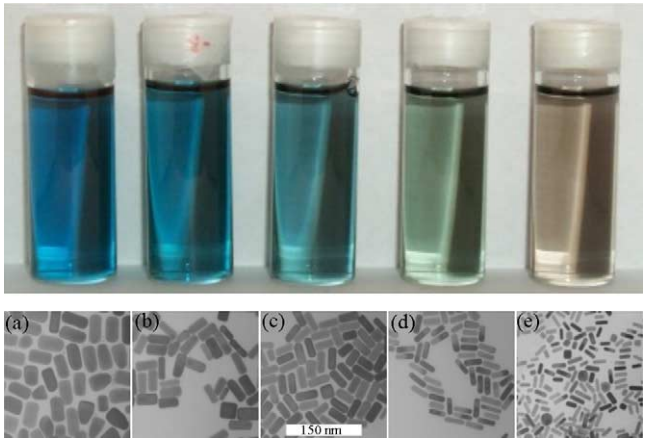

Fig. 2.4. The color of gold rods and the respective micrographs. The color changes take place for very small changes in mean aspect ratio.

origins of this will be discussed later. From Eq. (2.15), the enhanced sensitivity of gold rods over gold spheres towards dielectric perturbations is readily understood.

$$\alpha_{x,y,z} = \frac{4\pi abc(\varepsilon_{\mathrm{Au}} - \varepsilon_{\mathrm{m}})}{3\varepsilon_{\mathrm{m}} + 3L_{x,y,z}(\varepsilon_{\mathrm{Au}} - \varepsilon_{\mathrm{m}})} \tag{2.17}$$

$$3\varepsilon_{\mathrm{m}} + 3L(\varepsilon_{\mathrm{Au}} - \varepsilon_{\mathrm{m}}) = 0 \tag{2.18}$$

$$\varepsilon_{\mathrm{m}} + L\left(\varepsilon^0 - \frac{\lambda^2}{\lambda_{\mathrm{p}}^2} - \varepsilon_{\mathrm{m}}\right) = 0 \tag{2.19}$$

It follows that the peak position shifts according to:

$$\lambda^2 = \lambda_{\mathrm{p}}^2\left(\varepsilon^0 + \varepsilon_{\mathrm{m}}\left(\frac{1}{L} - 1\right)\right) \tag{2.20}$$

As the eccentricity of the rods increases, the slope of the dispersion curve increases. The longer the rod, the greater the sensitivity to refractive index effects on $\mathrm{SP_{long}}$. This holds provided that the ellipsoid model remains valid. However, such long rods will necessarily absorb in the IR, so that the color effect will be less apparent to the observer.

2.5. The effect of a shell layer

To tackle some of the key optical effects observed during synthesis and measurements of chemically fabricated metal nanorods, we can consider some simple modifications to Eqs. (2.10)–(2.16). In particular, the effect of a dielectric shell is important. Eq. (2.15) can be modified in the case of a small coated ellipsoid in the electrostatic limit. The polarizability is then given by:

$$\alpha^x = V\frac{\begin{array}{c}((\varepsilon_2 - \varepsilon_{\mathrm{m}})[\varepsilon_2 + (\varepsilon_1 - \varepsilon_2)(L^x_{\mathrm{core}} - fL^x_{\mathrm{shell}})] \\ +f\varepsilon_2(\varepsilon_1 - \varepsilon_2))\end{array}}{\begin{array}{c}([\varepsilon_2 + (\varepsilon_1 - \varepsilon_2)(L^x_{\mathrm{core}} - fL^x_{\mathrm{shell}})][\varepsilon_{\mathrm{m}} \\ +(\varepsilon_2 - \varepsilon_{\mathrm{m}})L^x_{\mathrm{shell}}]\varepsilon_2(\varepsilon_1 - \varepsilon_2))\end{array}} \tag{2.21}$$

Here, $\varepsilon_{\mathrm{core}}$ and $\varepsilon_{\mathrm{shell}}$ are the dielectric function of the core and shell components of the ellipsoid, ε_{m} is the real dielectric constant of the non-absorbing medium. L_{core} and L_{shell} are

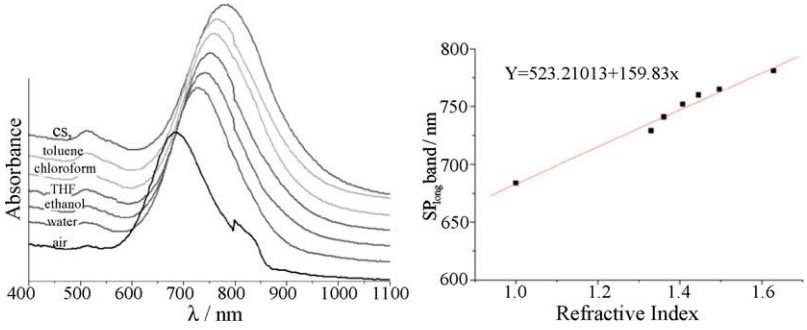

Fig. 2.5. Experimental spectra of gold nanorods in different solvents (left) and change in the longitudinal plasmon band position with refractive index (right). To obtain $n = 1$, the particles were coated on glass. However, the effective refractive index for small particles in air supported on glass is approximately $n_{\mathrm{eff}} = (n_{\mathrm{air}} + n_{\mathrm{glass}})/2 \sim 1.25$.

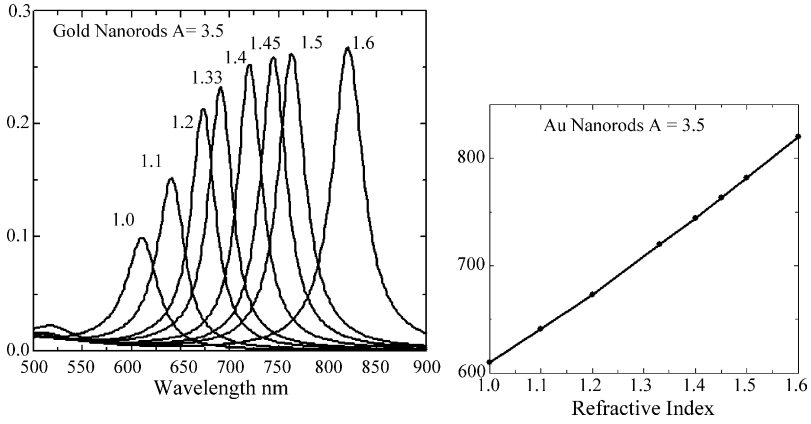

Fig. 2.6. Calculated spectra for gold ellipsoids with an aspect ratio of 3.5 in different media as a function of the medium refractive index. There is a drastic red-shift with increasing solvent polarizability. The peak in extinction coefficient occurs because at longer wavelengths, there is increasing damping, i.e., a rise in the value of ε'', see Fig. 2.1.

the depolarization factors for the core and shell, respectively, $V = 4\pi a_{\text{shell}} b_{\text{shell}} c_{\text{shell}}/3$ is the volume of the coated particle, f is the volume fraction $a_{\text{core}} b_{\text{core}} c_{\text{core}}/a_{\text{shell}} b_{\text{shell}} c_{\text{shell}}$ occupied by the inner ellipsoid. When $\varepsilon_{\text{core}} = \varepsilon_{\text{shell}}$, we recover Eq. (2.15) as expected.

The effect of the thin non-absorbing shell is similar to the effect of immersion in a medium with the same refractive index, and the origin of the spectral shift is similar. Because of the sensitivity of the surface plasmon resonance to both geometric and dielectric effects, particles in which there can be selective deposition or dissolution of a coating layer have promising applications as sensors. The peak position changes perceptibly even for thin shells. Any shell layer with a different refractive index to the embedding medium will cause a shift in the surface plasmon transverse and longitudinal mode positions. For example, an antibody functionalized gold rod will respond to the presence of the corresponding antigen through a red-shift in the plasmon mode, since the antigen will have a higher refractive index than water. However, there are other reasons for synthesizing core-shell nanorods. In order to stabilize gold rods against coalescence, and to facilitate dispersion and orientation in polymers, glasses or non-polar solvents, silica coating is particularly useful. In Fig. 2.7, we show calculated spectra for a silica-coated gold rod in water. The rod has dimensions 12 nm × 30 nm. The calculation shows the shift in SPL for 2, 4, 6 and 8 nm silica shells with an assumed refractive index of $n = 1.5$.

2.6. Orientation effects

Since the longitudinal and transverse localized plasmon resonances of gold nanorods are basically independent of each other, they can be selectively excited by using light polarized with the oscillating electric field parallel and perpendicular to the long axis of the rod, respectively. Experimentally, this effect can only be studied if all rods are oriented in the same direction, so that they respond equally to light with the same polarization, which can be realized through extension in polymer films [32]. Assuming the particles are small, the extinction coefficient of the film should be given by:

$$C_{\text{ext}} = kI\text{m}\{\alpha_{\text{L}}(1 - \cos^2(\theta)) + \alpha_{\text{T}}(\cos^2(\theta))\} \tag{2.22}$$

Typical calculated spectra for such a film as a function of the polarization of the incident light are shown in Fig. 2.8.

When the incident beam is polarized parallel to the long axis of the rods (0°), only the longitudinal surface plasmon

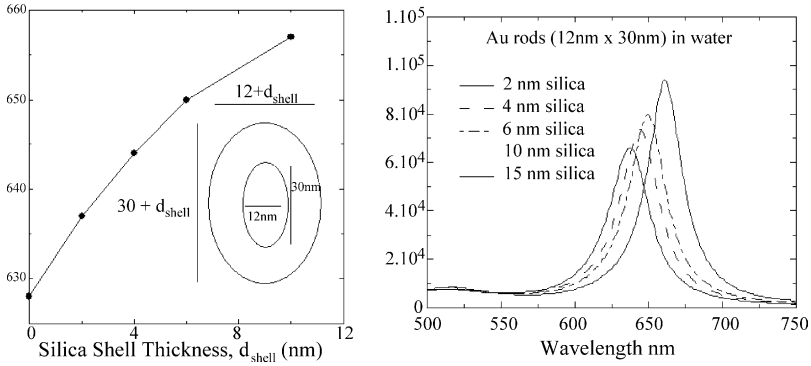

Fig. 2.7. Calculated spectra for a gold rod in water. The rod has dimensions 12 nm × 30 nm. The calculation shows the shift in SPL for 2, 4, 6, and 8 nm silica shells with an assumed refractive index of $n = 1.5$. Dielectric data from Weaver et al. [31]. Bulk gold assumed.

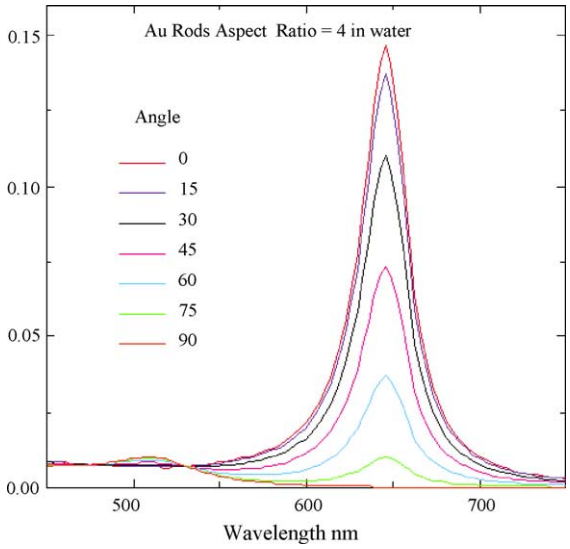

Fig. 2.8. Calculated spectra of vertically oriented gold nanorods with aspect ratio of 4.0 in water. The spectra are calculated for various angles, and show that there is an isosbestic point at about 530 nm.

is excited, and thus only the band at 645 nm is observed. Conversely, for light polarized perpendicular to the long axis (90°), the SP_{long} band is completely removed and only the transverse mode is excited. For intermediate angles, contributions of both modes exist, as defined by Eq. (2.22), which is confirmed by the presence of an isosbestic point at about 530 nm.

3. Synthesis and mechanism for Au nanorod formation

We now examine the three main methods used to produce gold rods through wet chemistry. Chronological order is followed, which in turn implies successive improvement in material quality. Each new method is also accompanied by a decrease in difficulty of the synthesis.

3.1. Template method

The template method for the synthesis of gold nanorods was first introduced by Martin and co-workers [33–35]. The method is based on the electrochemical deposition of Au within the pores of nanoporous polycarbonate or alumina template membranes. These authors showed that the Au/alumina composites can be optically transparent in the visible and also that by changing the aspect ratio of the prepared nanocylinders; the color of the composite membrane can be varied [25,36]. Initially, the template method was employed to prepare microscopic electrodes by depositing Au on a polycarbonate membrane using electrochemical plating methods [37]. Subsequently, the method has been applied not only to the synthesis of nanocomposites but also to the redispersion of the template-synthesized gold nanorods into water [38]. Alternatively, the rods could be dispersed into organic solvents through the dissolution of the appropriate membrane followed by polymer stabilization [39].

Schematically, the method can be explained as follows: initially a small amount of Ag or Cu is sputtered onto the alumina template membrane to provide a conductive film for electrodeposition. This is then used as a foundation onto which the Au nanoparticles can be electrochemically grown (stage I in Fig. 3.1). Subsequently, Au is electrodeposited within the nanopores of alumina (stage II). The next stage involves the selective dissolution of both the alumina membrane and the copper or silver film, in the presence of a polymeric stabilizer such as poly(vinylpyrrolidone) (PVP) (III and IV in the Fig. 3.1). In the last stage, the rods are dispersed either in water or in organic solvents by means of sonication or agitation.

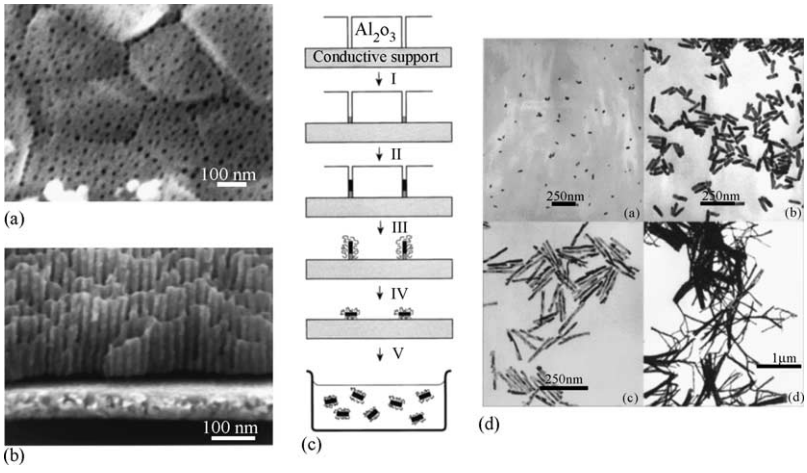

Fig. 3.1. (a and b) FEG–SEM images of an alumina membrane. (c) Schematic representation of the successive stages during formation of gold nanorods via the template method. (d) TEM micrographs of gold nanorods obtained by the template method. Reprinted with permission from reference [28]. © 2000 American Chemical Society.

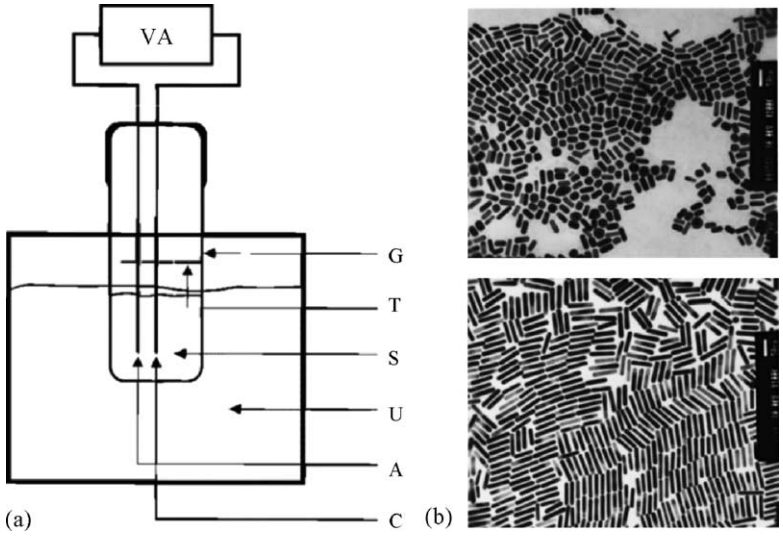

Fig. 3.2. (a) Schematic diagram of the set-up for preparation of gold nanorods via the electrochemical method containing; VA, power supply; G, glassware electrochemical cell; T, teflon spacer; S, electrode holder; U, ultrasonic cleaner; A, anode; C, cathode. (b) TEM micrographs of Au nanorods with different aspect ratios 2.7 (top) and 6.1 (bottom). Scale bars represent 50 nm. Reprinted with permission from ref. [49]. © 1999 American Chemical Society.

The diameter of the gold nanoparticles thus synthesized coincides with the pore diameter of the alumina membrane. This means, that Au nanorods with different diameters can be prepared by controlling the pore diameter of the template [40,41]. The length of the nanorods can be controlled through the amount of gold deposited within the pores of the membrane [28].

Similar techniques, though using different membranes, have been successfully applied to the synthesis of gold nanotubes [42–44], and nanostructured composites, including tubular composites, which comprise coaxial nanotubes made of different materials [45–48]. The fundamental limitation of the template method is the yield. Since only monolayers of rods are prepared, even milligram amounts of rods are arduous to prepare. Nevertheless, many basic optical effects could be confirmed through these initial pioneering studies.

3.2. Electrochemical methods

An electrochemical route to gold nanorod formation was first demonstrated by Wang and co-workers [26,49]. Their approach extended previous studies on the electrochemical synthesis of transition metal clusters within reverse micelles in organic solvent systems [50]. The method provides a synthetic route for preparing high yields of Au nanorods.

The synthesis is conducted within a simple two-electrode-type electrochemical cell, as shown in the schematic diagram in Fig. 3.2. A gold metal plate (typically 3.0 cm × 1.0 cm × 0.05 cm) is used as a sacrificial anode whilst the cathode is a platinum plate with similar dimensions. Both electrodes are immersed in an electrolytic solution containing a cationic surfactant, hexadecyltrimethylammonium bromide (C_{16}TAB), and a small amount of a much more hydrophobic cationic surfactant, tetradodecylammonium bromide (TC_{12}AB), which acts as a rod-inducing cosurfactant. The C_{16}TAB serves not only as the supporting electrolyte but also as the stabilizer for the nanoparticles, to prevent their further aggregation. The electrolytic cell containing the mixed solution is then placed inside an ultrasonic bath at 36 °C. Before the electrolysis, appropriate amounts of acetone and cyclohexane are added into the electrolytic solution. Acetone is used for loosening the micellar framework facilitating the incorporation of the cylindrical-shape-inducing cosurfactant into the C_{16}TAB micelles, and cyclohexane is necessary for enhancing the formation of elongated rod-like C_{16}TAB micelles [51]. A controlled-current electrolysis is used throughout the process with a typical current of 3 mA and a typical electrolysis time of 30 min.

During the synthesis, the bulk gold metal anode is initially consumed, forming $AuBr_4^-$. These anions are complexed to the cationic surfactants and migrate to the cathode where reduction occurs. It is unclear at present whether nucleation occurs on the cathode surface or within the micelles. Sonication is needed to shear the resultant rods as they form away from the surface or possibly to break the rod off the cathode surface. Another important factor controlling the aspect ratio of the Au nanorods is the presence of a silver plate inside the electrolytic solution, which is gradually immersed behind the Pt electrode. The redox reaction between gold ions generated from the anode and silver metal leads to the formation of silver ions. Wang and co-workers found that the concentration of silver ions and their release rate determined the length of the nanorods. The complete mechanism, as well as the role of the silver ions, is still unknown.

3.3. Seeded growth method

Seeded growth of monodisperse colloid particles dates back to the 1920s. More recently, the use of seeds to make more monodisperse metal nanoparticles has been reported

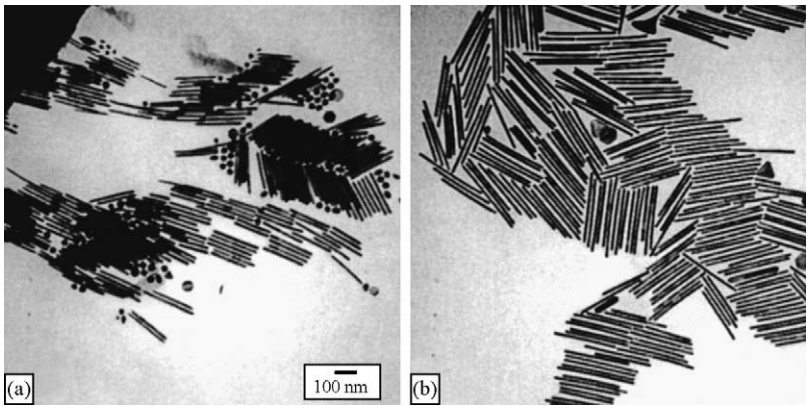

Fig. 3.3. TEM images of shape-separated 13 (a) and 18 (b) aspect ratio gold nanorods prepared by the seed-mediated method. Reproduced with permission from ref. [61]. © 2001 American Chemical Society.

by various authors [52,53]. Natan and co-workers proposed a seed-mediated approach to grow preformed, spherical gold nanoparticles in solution, based on the gold colloid surface-catalyzed reduction of Au^{3+} by hydroxylamine (a weak reducing agent that favors the reduction of Au ions at metallic surfaces). Alternatively, seeds could be grown using sodium citrate as a reductant [54–56], producing Au nanoparticles with diameters between 20 and 100 nm of improved monodispersity relative to the original Frens method [54]. These authors already pointed out that iterative hydroxylamine seeding leads to the formation of a distinct population (5–10%) of colloidal gold rods [55].

Jana et al. studied the growth of citrate stabilized gold nanoparticles (12 nm) by the seed-mediated method using a wide range of reducing agents and conditions [57]. They showed that even in the presence of seeds additional nucleation takes place [58]. Additional nucleation can be avoided by controlling critical parameters such as the rate of addition of reducing agent to the metal seed and metal salt solution and the chemical reduction potential of the reducing agent. A step-by-step particle enlargement method also allows a large seed to metal salt ratio to be maintained throughout successive growth steps [57]. Using this approach, Murphy and co-workers were able to prepare spherical particles in a size range 5–40 nm with relatively uniform size [59]. The primary nuclei were 3.5 nm gold seeds prepared by borohydride reduction of gold salt in the presence of citrate as capping agent [60]. The growth steps were carried out in aqueous surfactant media. Secondary nucleation during the growth stage was inhibited by carefully controlling the growth conditions, and in particular by using ascorbic acid as a weak reducing agent, that cannot reduce the gold salt in the presence of the micelles if the seed is not present.

By controlling the growth conditions in aqueous surfactant media it was possible to synthesize gold nanorods with tunable aspect ratio. It was found that addition of $AgNO_3$ influences not only the yield and aspect ratio control of the gold nanorods but also the mechanism for gold nanorod formation and correspondingly its crystal structure (see Section 4). At this point, it is thus convenient to differentiate seed-mediated approaches performed in the absence or in the presence of silver nitrate. As discussed below, it now seems that silver nitrate affects not just the yield of gold rods, but also plays a role in determining crystal structure, morphology and optical properties.

3.3.1. *Synthesis without $AgNO_3$*

Murphy and co-workers were able to synthesize high aspect ratio cylindrical nanorods using 3.5-nm gold seed particles prepared by sodium borohydride reduction in the presence of citrate, through careful control of the growth conditions, i.e., through optimization of the concentration of C_{16}TAB and ascorbic acid, and by applying a two- or three-step seeding process (see Fig. 3.3). The yield of the nanorods thus synthesized is ca. 4% [61]. The long rods can be concentrated and separated from the spheres and excess surfactant by centrifugation. Later, the same group reported an improved methodology to produce monodisperse gold nanorods of high aspect ratio in ∼90% yield [62], just through pH control. In the new proposed protocol, the pH of the growth solution was changed from 2.8 to 3.5 and 5.6, which led to the formation of gold nanorods of aspect ratio 18.8 ± 1.3 and 20.2 ± 1.2, respectively. The newer procedure also, resulted in a dramatic increase in the relative proportion of nanorods and reduced the separation steps necessary to remove smaller particles.

The mechanism of formation of rod-shaped nanoparticles in aqueous surfactant media remains unclear. Based on the idea that C_{16}TAB absorbs onto gold nanorods in a bilayer fashion, with the trimethylammonium headgroups of the first monolayer facing the gold surface [63], Murphy and co-workers [64] proposed that the C_{16}TAB headgroup preferentially binds to the crystallographic faces of gold existing along the sides of pentahedrally twinned rods, as compared to the faces at the tips (see Section 4). The growth of gold nanorods would thus be governed by preferential adsorption of C_{16}TAB to different crystal faces during the growth, rather than acting as a soft micellar template [64]. The influence of C_nTAB analogues in which the length of the hydrocarbon tails was varied, keeping the headgroup and the counterion constant was also studied [65]. It was found that the length

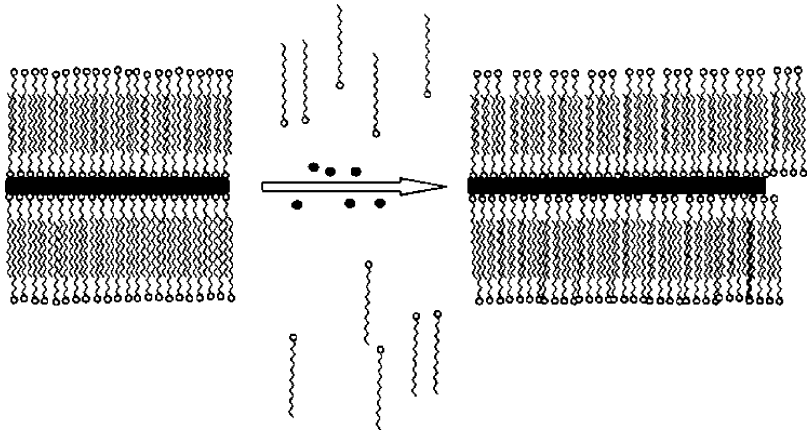

Fig. 3.4. Schematic representation of "zipping": the formation of the bilayer of C_nTAB (squiggles) on the nanorod (black rectangle) surface may assist nanorod formation as more gold ions (black dots) are introduced. Reproduced with permission from ref. [65]. © 2003 American Chemical Society.

of the surfactant tail is critical for controlling not only the length of the nanorods but also the yield, with shorter chain lengths producing shorter nanorods and longer chain lengths leading to longer nanorods in higher yields. Considering the preferential adsorption of C_{16}TAB to the different crystal faces in a bilayer fashion [63–66], a "zipping" mechanism was proposed taking into account the van der Waals interactions between surfactant tails within the surfactant bilayer, on the gold surface, that may promote the formation of longer nanorods from more stable bilayers (see Fig. 3.4) [65].

Recently, Pérez-Juste et al. investigated the factors affecting the nucleation and growth of gold nanorods under similar conditions [29]. They showed that when temperature and C_{16}TAB concentration are reduced, it is also possible to synthesize short aspect ratio (between 1 and 6) gold nanorods with a yield up to ~50%. The control of the aspect ratio, as well as the monodispersity and the yield were demonstrated to be influenced by a number of factors, such as the stability of the seed, temperature and the nature and concentration of surfactant. The yield of nanorods prepared from C_{16}TAB capped seeds is much higher than that from naked (or citrate stabilized) seeds (see Fig. 3.5). This indicates that the more colloidally stable the gold seed nanoparticles are, the higher the yield of rods. As expected, the lower the amount of seed added the higher the aspect ratio of the nanorods formed. The increase in the aspect ratio implies a red-shift of the longitudinal plasmon band (as explained in Section 2), see Fig. 3.5.

Pérez-Juste et al. proposed an electric-field-directed growth of gold nanorods in aqueous surfactant solutions [29]. The proposed mechanism is based on a series of observations related to the binding of the gold salt ions to the cationic micelles:

(a) The yield of rods improves with increasing colloidal stability of the seeds, hence dimers or coalescence are not precursors to rod formation.
(b) Bromide ion is much better than Cl^- as a rod-inducing agent in the presence of C_nTA^+. As the length of the surfactant tail, C_n, increases the yield and the aspect ratio of the nanorods are increased [65]. The addition of NaCl, $NaNO_3$, or NaBr reduces the aspect ratio of the nanorods, the effect being similar for each ion. An increase in the ionic strength produces a decrease in the yield of rods.
(c) Under optimal conditions, the aspect ratio can be controlled through seed to $HAuCl_4$ ratios, since there is little nucleation of new particles. An increase in the amount of

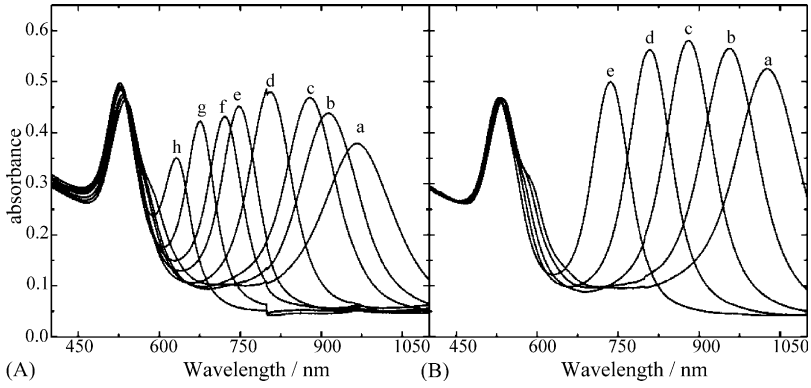

Fig. 3.5. UV–vis–NIR spectra of gold nanorods prepared with citrate capped (A) and C_{16}TAB capped (B) gold seeds. Reproduced with permission from ref. [29]. © 2004 Wiley-VCH.

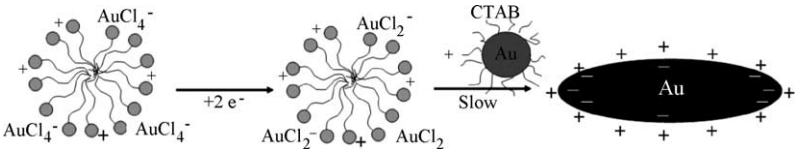

Fig. 3.6. Mechanism for gold nanorod formation. The transport of the gold ions bound to the C_{16}TAB micelles to the growing seed particles is controlled by the double layer interaction. Reproduced with permission from ref. [29]. © 2004 Wiley-VCH.

seed solution added means a decrease in the aspect ratio of the rods.

(d) Both $AuCl_4^-$ and $AuCl_2^-$ are quantitatively adsorbed to C_{16}TAB [67]. The optimal C_{16}TAB:$HAuCl_4$ concentration ratio is in a narrow window since precipitation of C_{16}TAB–$HAuCl_4$ occurs at <10:1 ratios. This can be avoided by increasing the temperature. However, the yield of rods decreases gradually at higher temperatures.

(e) The presence of C_{16}TAB not only directs Au to the tips, but also drastically retards the rate of metallic gold formation compared with the absence of C_{16}TAB [57]. The higher the curvature of the gold surface, the faster the rate of growth.

In the presence of C_{16}TAB, ascorbic acid reduces Au^{III} to Au^{I} via reaction (3.1). However, no colloidal gold is formed, i.e., disproportionation of $AuCl_2^-$–C_{16}TAB does not occur (reaction (3.2)). In fact, it is possible to prepare solutions of $AuCl_2^-$–C_{16}TAB by adding $HAuCl_4$ to colloidal gold in the presence of C_{16}TAB [68]. Consequently, the reduction of Au^{I} can proceed through electron transfer at the surface of the electron-rich gold seeds (reaction (3.3)). In the presence of C_{16}TAB, the reduction can be described by reaction (3.4).

$$AuCl_4^- + 2e^- \rightleftarrows AuCl_2^- + 2Cl^- \quad (3.1)$$

$$3AuCl_2^- \rightleftarrows AuCl_4^- + 2Au^0 + 2Cl^-; \quad K = 15.5\times10^7 \quad (3.2)$$

$$AuCl_2^- + e^- \rightleftarrows 2Au^0 + 2Cl^- \quad (3.3)$$

$$AuCl_2^- - CTAB_{mic} + Au_m \rightleftarrows Au_{m+1} - CTAB_{mic} + CTAB_{mic} + 2Cl^- \quad (3.4)$$

During the typical microelectrode-type deposition [69], electrons are transferred to the gold particle while adsorbed $AuCl_2^-$ ions may pick up electrons at any favorable adsorption site. Usually spherical growth is obtained under these circumstances [54,69], but in the case of C_{16}TAB containing solutions, the gold seeds are encapsulated in C_{16}TAB, and the gold ions are likewise bound to C_{16}TAB [67]. The Zeta potential of C_{16}TAB micelles and the C_{16}TAB-coated gold surfaces are both around +90 mV [70]. It was postulated that the rate of nanorod formation is determined by the frequency of collisions of $AuCl_2^-$ laden cationic micelles with the cationic gold seed particles (see Fig. 3.6). This interaction will be controlled by the electrical double layer interaction between micelles and gold nanorods. The rate of the reaction is then controlled by the collisions of the micelles. A faster rate of collision of the micelles at the tips than at the sides will induce rod formation, which was confirmed through calculations of the potential distribution and potential gradient around an ellipsoid [29]. These calculations showed that the potential decays more rapidly near the tip, which means that it will be easier for a micelle to approach to a given distance at the tip rather than from the sides of the rods. The initial change in morphology could only be explained assuming that a stacking fault or twinning plane in

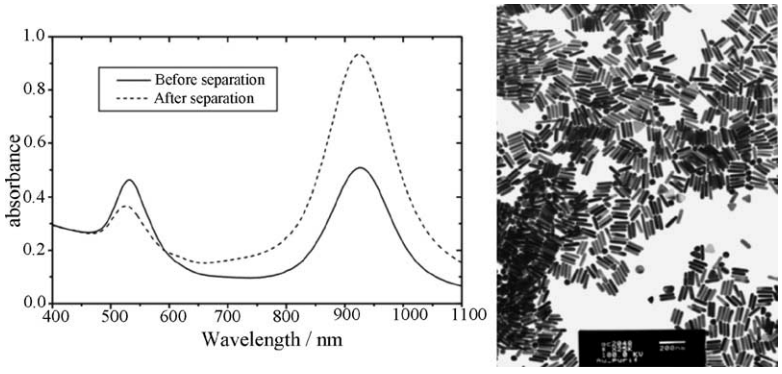

Fig. 3.7. UV–vis–NIR spectra of nanorod solutions before and after shape separation. Concentration of gold is the same in both solutions and equal to 1.25×10^{-4} M (left). TEM image of shape separated short nanorods (aspect ratio ~4.30) (right).

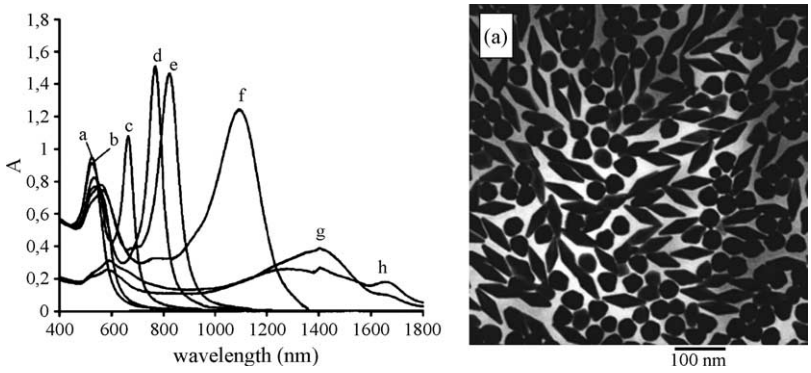

Fig. 3.8. UV–vis spectra of Au nanorods with increasing aspect ratios (a–h) formed by decreasing the amount of added seed (left). TEM image of Au nanorods synthesized in the presence of silver nitrate (right). Adapted with permission from refs. [81] and [82], respectively. © 2001 and 2002 American Chemical Society.

the seed should be present to create an initial electric field asymmetry.

These relatively monodisperse gold nanorods can be separated from small size spheres by centrifugation but this separation method is not successful for rods and spheres with similar sizes. Other separation methods, such as size selective precipitation and extraction methods, commonly used to separate mixtures of different size nanospheres (in the size range 1–10 nm) [71,72], do not work for nanorods because of their larger sizes. Shape separation based on nanoporous filters also fails because the short axis of the nanorods and spheres have similar diameters. Wang and co-workers used size exclusion chromatography to separate nanorods from spheres but only a partial separation was possible [73]. An exciting prospect is the phase separation technique devised by Jana for the isolation of single size nanorods from a mixture of rods, spheres and plates with different size [74]. Separation is achieved through surfactant assisted ordering of nanorods in concentrated dispersions (see Fig. 3.7). Theoretical and experimental studies have shown that ordered liquid crystalline phases could be formed in concentrated dispersions of anisotropic colloid particles [75–79]. In a concentrated dispersion, gold nanorods form liquid crystalline, ordered structures [80] and precipitate out of solution. Liquid crystalline ordering is enhanced through nanoparticle shape anisotropy, resulting in different precipitation conditions for spheres, plates and short gold nanorods, so that conditions can be manipulated for successful separations [74].

3.3.2. Synthesis with $AgNO_3$

The presence of silver nitrate allows better control of the shape of gold nanorods synthesized by the electrochemical method, and Murphy and co-workers proposed a variation of their initial procedure for long nanorods [61], in order to increase the yield of rod-shaped nanoparticles (up to 50%) and to control the aspect ratio of shorter nanorods and spheroids [81]. Under identical experimental conditions, a small amount of silver nitrate is added (5×10^{-6} M) prior to the growth step. The aspect ratio of the spheroids and nanorods can be controlled by varying the ratio of seed to metal salt, as indicated in the spectra of Fig. 3.8. The presence of the seed particles is still crucial in the growth process, and there is an increase in aspect ratio when the concentration of seed particles is decreased.

The mechanism by which Ag^+ ions modify the metal nanoparticle shape is not really understood. It has been hypothesized that Ag^+ adsorbs at the particle surface in the form of AgBr (Br^- coming from C_{16}TAB) and restricts the growth of the AgBr passivated crystal facets [81]. The possibility that the silver ions themselves are reduced under these experimental conditions (pH ~2.8) can be neglected since the reducing power of ascorbate is too positive at low pH [83]. As shown in Fig. 3.8, the presence of silver nitrate induces formation of short gold nanorods with a needle-like shape, in contrast to the spherical capped ends of high aspect ratio rods synthesized in the absence of Ag^+ (Fig. 3.3) and in multistep synthesis. This shape effect depends not only on the presence of $AgNO_3$, but also on the nature of the seed solution.

Nikoobakht and El-Sayed developed a new variation of the seed-mediated growth method, where the drawbacks and limitations of the earlier methods, such as formation of non-cylindrical nanorods, ϕ-shaped particles and contamination by spherical particles, were overcome essentially by the use of C_{16}TAB-capped rather than citrate-capped seeds [84]. This resulted in the formation of 99% gold nanorods with aspect ratios, which could be tuned from 1.5 up to 5. The replacement of sodium citrate with C_{16}TAB in the seed formation step produces small spherical particles (<4 nm) [84]. Differences in yield and shape of the nanorods could be due to the slightly different size of the C_{16}TAB and sodium citrate capped seeds, but it may also be attributed to a different crystal structure in the two kinds of seed particles. A detailed HRTEM analysis is needed to clarify this point.

By simply adjusting the amount of silver ions in the growth solution, a fine-tuning of the aspect ratio of the nanorods can be achieved, so that an increase in silver concentration (keeping the amount of seed solution constant) leads to a red-shift in the longitudinal plasmon band. There is, however, a critical silver ion concentration, above which the aspect ratio of the nanorods decreases again [84]. Interestingly, the

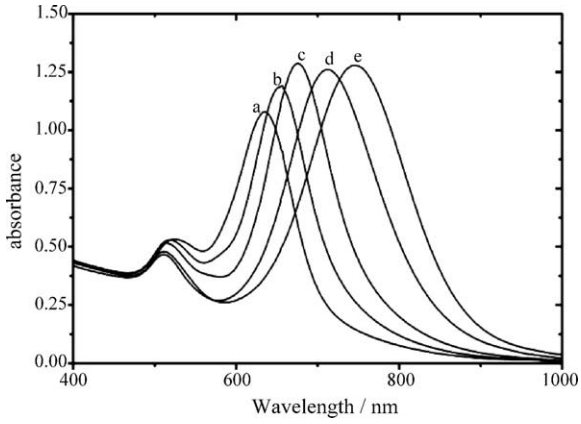

Fig. 3.9. UV–vis spectra of Au nanorods prepared in the presence of silver nitrate by the El-Sayed's protocol. The corresponding TEM images can be seen in Fig. 2.4. Reproduced from ref. [85].

aspect ratio can also be controlled by adjusting the amount of seed solution added to the growth solution in the presence of constant Ag^+ concentration [85]. Contrary to expectations, an increase in the amount of seed produces a red-shift in the longitudinal plasmon band position, as shown in Fig. 3.9, pointing toward an increase in aspect ratio. From the TEM images in Fig. 2.4 it can be observed that while the length of the nanorods decreases slightly, the width decreases further with increasing concentration of seed added [85,86].

A similar trend is observed when the gold ion concentration is increased [86]. Nanorods with higher aspect ratios could be obtained for gold ion concentrations up to $[Au^{3+}] \sim 6.0 \times 10^{-4}$ M. The concentration of ascorbic acid has also been shown to influence the morphology, with decreasing length and rod yield observed for increasing ascorbic acid concentrations, when all other parameters are kept constant. This effect has been attributed to a fast supply of substrate to the seeds in the presence of a large excess of reducing agent [86].

By adjusting the silver ion or gold seed concentrations in this single-component surfactant (C_{16}TAB) solution, the longitudinal plasmon band can be tuned up to 825 nm, corresponding to an aspect ratio of ∼4.5. To grow gold nanorods with larger aspect ratios (>5), Nikoobakht and El-Sayed proposed the use of a binary surfactant mixture containing C_{16}TAB and benzyldimethylammoniumchloride (BDAC) [84]. Two different approaches have been proposed: firstly, by changing the BDAC:C_{16}TAB ratio from 16 to 2, the aspect ratio of the nanorods can be tuned from 5 up to 8. The process in this binary mixture is complex. There is an initial fast growth stage that occurs over the first 1 h after addition. This is followed by a much slower growth step that takes place over a week. The approach presents two main disadvantages related to the ageing of the solutions, namely the low reproducibility and the formation of a large amount of spherical particles as the surfactant ratio is increased.

A second approach, which employs a low BDAC:C_{16}TAB surfactant ratio, has been used to ensure fewer nanospheres are formed. After the first stage of the growth is completed (fast growth step), different amounts of growth solution are added gradually. These gradual additions result in a red-shift of the longitudinal plasmon band position, which means that the length of the nanorods is increased each addition.

Before considering the possible growth mechanism in the presence of silver nitrate it is interesting to study how the presence of silver ions alters the growth kinetics. Fig. 3.10 shows the UV–vis spectra at different stages of the nanorod growth, both in the absence (left) and presence (right) of silver nitrate. In both cases, the seed-mediated growth kinetics are slower than those in the absence of C_{16}TAB [57]. In fact,

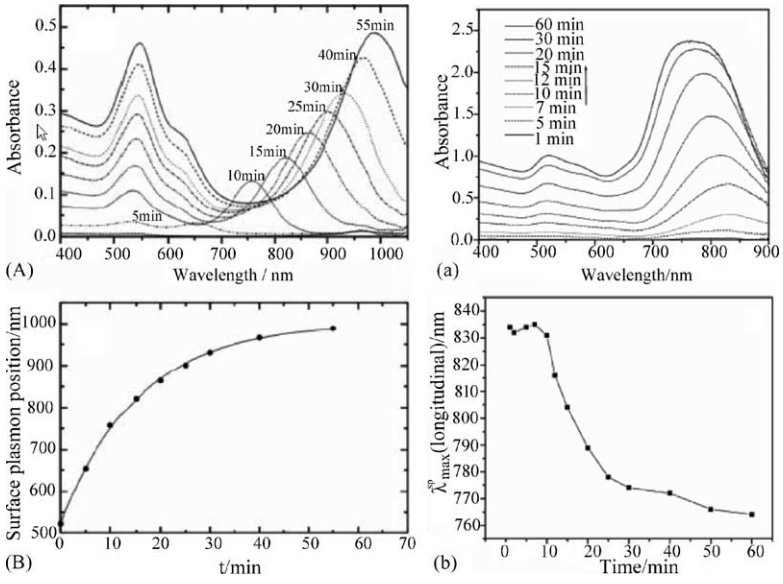

Fig. 3.10. UV–vis spectra (a) and position of the longitudinal plasmon band (b) at different stages of nanorod growth in the absence (left) and in the presence (right) of silver nitrate. Reproduced from refs. [29] and [86], respectively. © 2004 Wiley-VCH and American Chemical Society, respectively.

C_{16}TAB can retard the rate of gold reduction by a factor of 100–1000. The time evolution of the spectra, as well as the different crystallographic structures (see Section 4), suggest that the growth mechanisms are different. In the absence of silver ions, the position of the longitudinal plasmon band is clearly red-shifted as the gold ions are being reduced, meaning that the aspect ratio of the nanorods increases as long as there is gold salt precursor available. This is consistent with the preferential growth of the particles at the tips, as discussed above [52]. In the presence of silver ions, the longitudinal plasmon band is only apparent after 1 or 2 min, and surprisingly, it blue-shifts as the growth reaction proceeds. Sau and Murphy studied this evolution, and found that the aspect ratio, and therefore the length, increases quickly, but then slowly decreases over time as a consequence of a faster increase in width [86].

The mechanism in this case must be related to the presence of silver nitrate, since this is essential for the preparation of nanorods in high yields. While the role of silver ions is not clearly understood at this moment, two mechanisms have been proposed to account for gold nanorod formation.

In one mechanism, the surfactant forms a soft template, with a certain size that depends on surfactant concentration and ionic strength of the solution [84]. The growth solution contains a mixture of gold and silver ions, and when ascorbic acid is added only gold ions are reduced, since silver ions can only be reduced at basic pH values [83,87]. Nikoobakht and El-Sayed proposed that the silver ions located between the headgroups of the capping surfactant (C_{16}TAB) can be considered as Ag–Br pairs, decreasing the charge density on the bromide ions, and therefore, the repulsion between neighboring headgroups on the gold surface, and resulting in C_{16}TAB template elongation [84]. This possibility is supported by the stronger affinity of C_{16}TAB monomers for the side facets compare to the end facets [88]. High-resolution TEM images show that nanorods have four facets [89]. In the case of the BDAC:C_{16}TAB surfactant mixtures, the template is considered to be more flexible than the single component surfactant. Due to the larger affinity of C_{16}TAB monomers for the side facets, it has been assumed there is a higher probability of having BDAC monomers bound to the end facets of the nanorods, promoting a faster growth in the longitudinal direction, due to the weaker bonding in Ag–Cl pairs, relative to that in Ag–Br pairs [84].

The second mechanism considers a rigid structure of C_{16}TAB monomers, which helps maintain one-dimensional growth, but which also serves to control the rate of gold reduction [86], in a similar fashion to the mechanism previously proposed for the formation of long rods in the absence of silver ions (the “zipping” mechanism discussed above) [64]. As already pointed out, the silver ions will not be reduced by ascorbic acid, but will form silver bromide during the synthesis (bromide from C_{16}TAB). Murphy and co-workers proposed the adsorption of silver bromide to the facets of the gold nanocrystals, slowing down gold reduction and inducing single crystalline growth of the nanorods.

3.4. Other methods

Other methods have been proposed to account for the formation of gold nanorods. However, they only lead to low amounts, with low reproducibility and much difficulty in obtaining long rods in decent yields. We summarize here the ones we consider more relevant.

Yang and co-workers developed a photochemical method for the synthesis of gold nanorods [90], which is performed in a growth solution similar to that described for the electrochemical method [26], in the presence of different amounts of silver nitrate and with no chemical reducing agent. Gold nanorod formation is induced instead by UV light irradiation. The aspect ratio increases when more silver ions are added, and this is accompanied by a decrease in rod width, while in the absence of silver ions, spherical particles are obtained. Therefore, the possibility of a rod-like micellar template mechanism can be discarded and these experiments indicate the critical role played by silver ions in determining the particle morphology. El-Sayed and co-workers suggested a growth mechanism similar to those of the standard methods (electrochemical, seed-mediated and photochemical). The mechanism proposes the addition of silver ions for controlling the aspect ratio, with the formation of one-dimensional gold nanostructures postulated to occur through a combination of nanocrystal aggregation and specific crystal face stabilization [91,92] induced by the presence of silver (or AgBr) [90].

In a related work, Yamada and co-workers found that the combination of chemical and photochemical methods leads to an acceleration in the rate of nanorod formation [93]. This protocol implies the addition of ascorbic acid prior to UV light irradiation, which produces the reduction of Au^{III} to Au^{I}. Nanorod formation is then accelerated by a factor of ca. 60 [93].

Markovich and co-workers adapted the seed-mediated method in the absence of silver nitrate proposed by Murphy and co-workers [61] for the growth of gold nanorods directly on mica surfaces [94]. The method involves the attachment of the spherical seed nanoparticles to a mica surface, which is then dipped in a C_{16}TAB surfactant growth solution. About 15% of the surface-bound seeds are found to grow as nanorods. This yield enhancement of nanorods, compared to that obtained for the solution growth technique (ca. 4%) [61], was attributed to a change in the probability of the growing seed to develop twinning defects. Subsequently, Wei et al. adapted the method to grow nanorods directly on glass surfaces [95]. They studied the influence of the linker used to attach the seed particles and the gold salt concentration in the growth solution on the formed gold nanostructures.

4. Structural characterization

At present there is some dispute over the growth direction of gold nanorods and the identity of the primary crystallo-

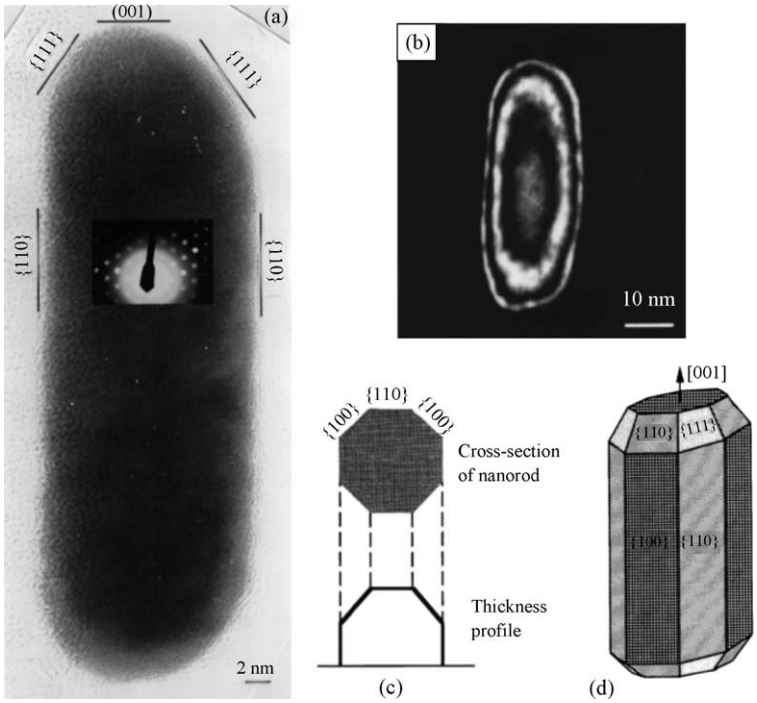

Fig. 4.1. (a) High-resolution TEM image of a gold nanorod showing the facetted crystal structure of the rod. The inset is the electron diffraction pattern, which confirms its single crystalline structure. (b) Dark-field TEM image of a gold nanorods. Cross-section and the corresponding profile of crystal thickness (c) as well as the structural model (d) proposed by Wang et al. for Au nanorods. Reproduced from ref. [89].

graphic facets exposed. Several different structures have been proposed. To date, thorough structural characterization has only been carried out for gold nanorods prepared by the electrochemical and seed-mediated (no silver nitrate) methods. In the following section, we attempt to clarify some of the key findings. This is important for two distinct reasons. Firstly, knowledge of the precise crystal structure sheds light on the mechanism of intervention by C_{16}TAB surfactant. Secondly, the material properties of metal nanorods and nanowires will depend strongly on the preferred growth direction.

4.1. Electrochemical method

Wang et al. studied the different crystallographic faces of gold nanorods with different aspect ratios prepared by the electrochemical method using high-resolution TEM (HRTEM) [88,89,96]. They distinguished between short rods, long rods and spherical nanoparticles present as final products. In the case of short rods, it was observed that the particles tend to align on the substrate after the solution dries out, with an even spacing between them. This self-assembly is not only related to a shape effect but also to the concentration and the uniform length of the surfactant capping molecules [79]. From the diffraction contrast, Wang et al. found that almost all of the short gold nanorods contain no stacking faults or twins, i.e., they are single crystals. The nanorods were found to be preferentially lying on the {1 1 0} face, though particles lying on {1 0 0} faces were also observed, suggesting that these ({1 0 0}) faces have smaller areas than the {1 1 0} faces [89].

Fig. 4.1a shows a HRTEM image of a single crystal gold nanorod oriented along the [1 1 0] direction. The faces enclosing the nanorods were identified from the electron diffraction pattern, the dominant side faces being {1 1 0} with the growth direction being [0 0 1], while the ends of the nanorods are terminated by the {0 0 1} and {1 1 1} faces, again with smaller areas. Wang et al. used the dark-field TEM technique to show the presence of {1 0 0} faces at the sides of the nanorods. If a nanorod is enclosed by {1 1 0} and smaller {1 0 0} faces, the fringes should not be equally spaced and there is a broad centre band (Fig. 4.1b). A comparison with the experimental image (Fig. 4.1a), showing a uniform band at the centre and unequally spaced fringes around it, suggests that the cross-section of the nanorod is consistent with that shown in Fig. 4.1c, and therefore the schematic representation of the geometrical structure of the nanorods corresponds to that shown in Fig. 4.1d.

Wang et al. also reported the presence of a small population of longer rods (2–4 μm in length) that coexist with the main population of short rods. Such long rods display a twin plane parallel to their axis, separating the rods into two halves along the axial direction (Fig. 4.2). The electron diffraction pattern indicates the presence of a twin parallel to the axial growth direction. Taking into account that face-centered cubic Au has {1 1 1} twin planes and that the growth direction must be parallel to the twin plane, they proposed a structural model for these nanorods where the {1 1 1} and {1 $\underline{1}$ 0} faces coexist.

Summarizing, Wang et al. showed that short gold nanorods prepared by the electrochemical method are single crystals with {1 1 0} and {1 0 0} as dominant faces, while the long

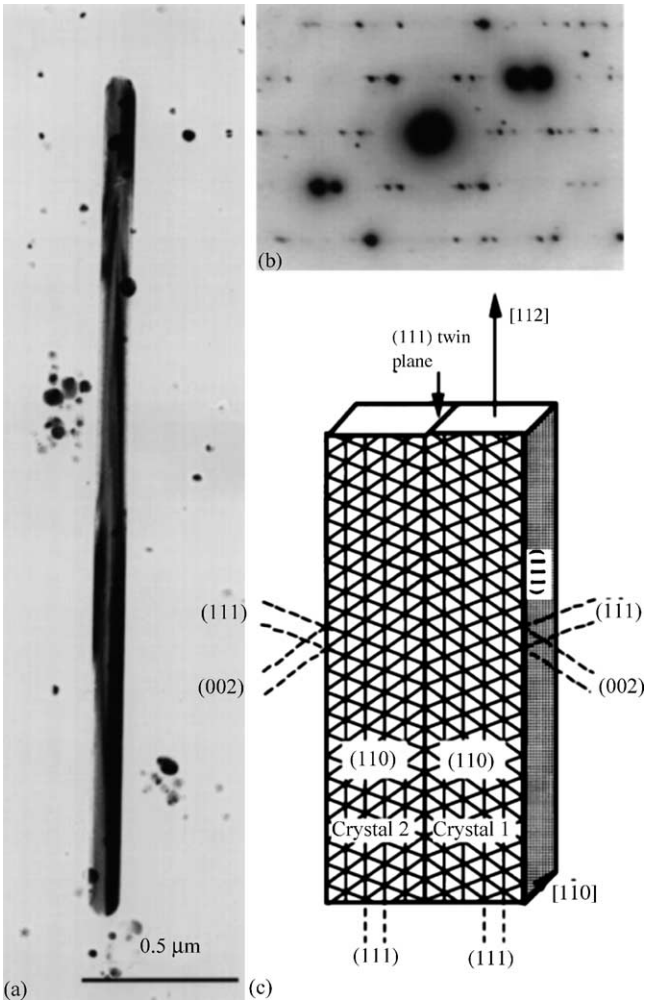

Fig. 4.2. (a) TEM image of a long nanorods; (b) the corresponding electron diffraction pattern; (c) the proposed structure model for long gold nanorods. Reproduced with permission from ref. [89].

rods present one twin with {1 1 1} and {1 1 0} as dominant faces.

4.2. Seed-mediated method

The gold nanorods prepared by the seed-mediated method in the absence of silver nitrate have been studied in more detail than those prepared in the presence of silver nitrate, basically because the synthetic protocol was proposed earlier [61,84]. Two different studies using TEM have been published dealing with the crystal structure, but slightly different results were obtained.

Gai and co-workers studied the atomic structure of long gold nanorods prepared by the seed-mediated method proposed by Murphy and co-workers [61] using an atomic resolution environmental transmission electron microscope (ETEM) [97–99] attached to a scanning-TEM (STEM) and equipped with a field emission gun [100]. This technique combines the atomic resolution imaging capability with atomic level chemical and crystallographic analyses. They found that all non-rod-shaped particles are multiply twinned, dominated by decahedral and icosahedral shapes. In the case of nanorods, they observed the presence of twin defect structures on the {1 1 0} crystal face, which is present along the [1 0 0] direction (Fig. 4.3A). The presence and the orientation of twin defects were confirmed by power electron nanodiffraction, which shows extra reflections along the [1 0 0] direction (Fig. 4.3B). TEM also demonstrated that the nanorods grow in the [1 0 0] directions with {1 1 0} faces bounded by {1 1 1} surfaces [101].

Based on these results, Gai and Harmer proposed a growth mechanism based on surface energy minimization being responsible for the nucleation and growth of the nanorods. Initially, multiply twinned particles are formed, and those twinned areas presenting weaker bonding favor gold deposition, leading to preferential growth. Fig. 4.3D shows a schematic representation of the proposed growth model. Since the {1 1 0} gold facets have a higher surface energy and therefore weaker atomic bonding, stronger bonding with the surfactant molecules was predicted, leading to the stabilization of those facets against crystal growth [101].

Mann and co-workers also studied the crystalline structure of gold nanorods prepared through the three-step seeding method proposed by Murphy and co-workers for the synthesis of long gold nanorods [61]. The studies were performed by selective area electron diffraction (SAED) in combination with HRTEM. In this case, none of the gold nanorods observed were single domain crystals. Instead, the electron diffraction patterns were consistent with a pentagonally twinned prism with five {1 0 0} side faces capped with five {1 1 1} faces at both ends, with growth again being observed to be along the [1 1 0] direction (Fig. 4.4a).

A similar study was subsequently performed in order to follow the evolution of particle size and shape throughout the multiple step process. The initial seed particles produced by sodium borohydride reduction in the presence of sodium citrate are single crystals [64]. In the first growth step, the addition of the seed to the growth solution produces isometric penta-twinned particles with well-defined {1 1 1} faces and {1 0 0} side faces arranged along the [110] direction. In the second step, the transfer of the primary gold rods to a fresh growth solution leads to further growth, but in addition, the transformation of a low percentage (ca. 4%) of the twinned particles into nanorods is observed. This low conversion percentage shows that the transformation from isotropic to anisotropic growth of the isotropic penta-twinned particles is not highly competitive. The next growth step increases the percentage of rod-shaped particles to ca. 10% due to the transformation into nanorods of ca. 6% of the particles that had grown as isometric particles in the previous step [64]. It is interesting to point out that once the rod-like shape is induced, the width of the nanorods increases just slightly as compared to the length, suggesting an autocatalytic anisometric growth [29]. Mann and co-workers proposed that this slow increase in width is due to the blocking of {1 0 0} faces from further growth as compared to the {1 1 1} end-faces, associated

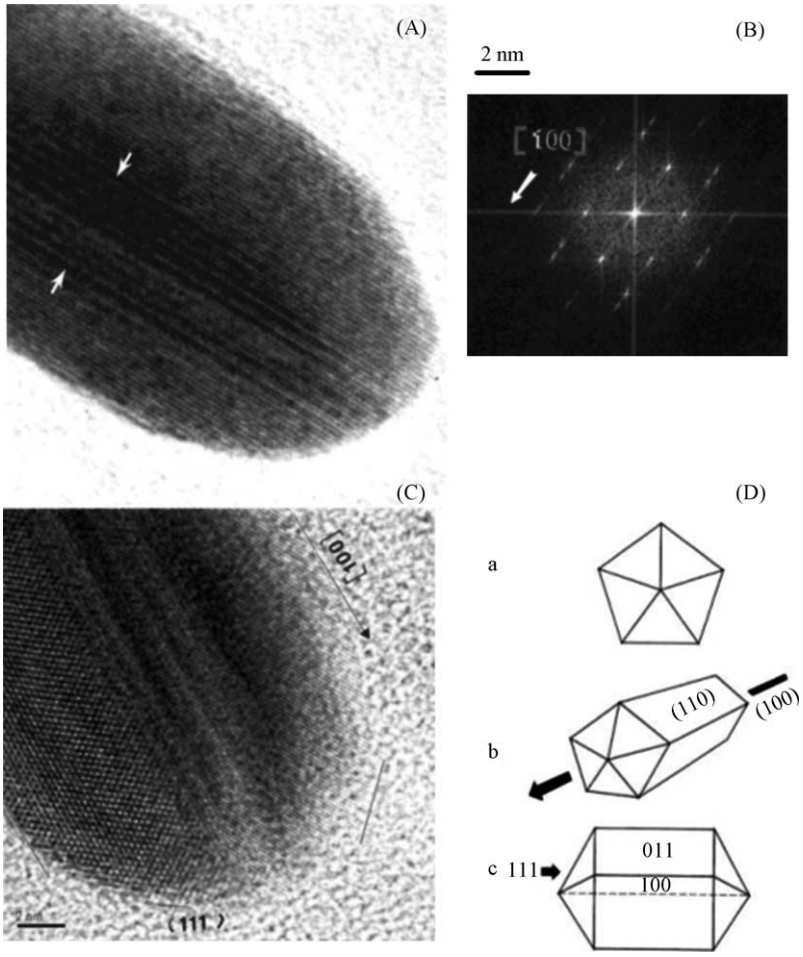

Fig. 4.3. (A) HRTEM image of a nanorod showing a twin defect on the {1 1 0} surface. The dimension of the twin lamellae is around 4 nm. (B) Power spectrum nanodiffraction from the twin region, showing additional reflections due to the twins along the [1 0 0] direction. (C) HRTEM image of a nanorod showing {1 1 0} and {1 1 1} faces and growth along [1 0 0] direction. (D) Model proposed by Gai et al. for nanorod growth: (a) initial multiple twinned particle; (b) growth along the [1 0 0] direction; (c) projections of a nanorod with {1 0 0} and {1 1 1} faces and [100] direction. Adapted with permission from ref. [101]. © 2002 American Chemical Society.

with the stronger binding to the sides in comparison to the end faces. The suggested mechanism involves a preferential interaction of the surfactant molecules with side faces facilitating a bilayer assembly of the surfactant molecules [63,65].

No structural characterization studies have been published to date for gold nanorods prepared by the seed-mediated method in the presence of silver nitrate reported by Nikoobakht and El-Sayed [84]. Nevertheless, from pre-

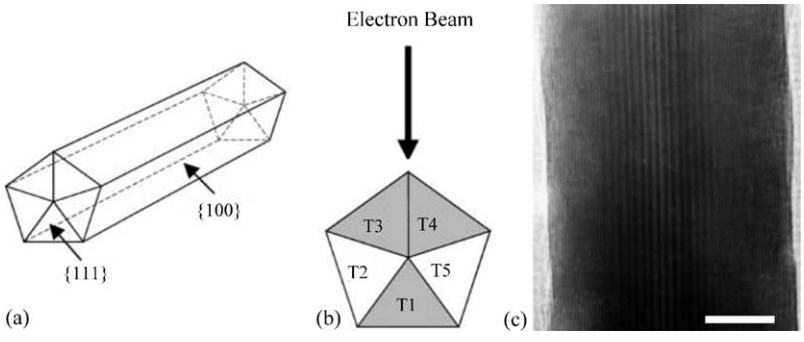

Fig. 4.4. (a) Schematic representation of the penta-twinned gold nanorod structure with (1 0 0) side faces and (1 1 1) end faces proposed by Mann and co-workers. (b) Cross-section of the nanorod structure showing the arrangements of the twins and possible orientation of domains with respect to the electron beam for the HRTEM image showed in (c). The wider stripes in the central region are due to double diffraction as a consequence of twin domains superposition. Adapted with permission from ref. [64]. © 2002 Royal Society of Chemistry.

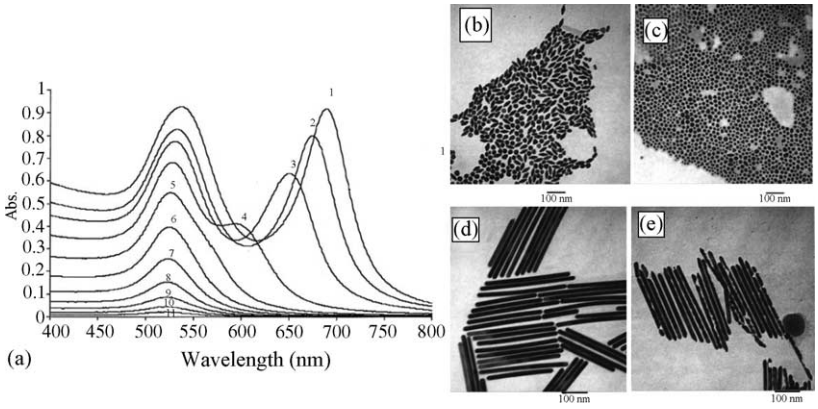

Fig. 5.1. (a) Time evolution of the UV–vis spectra during cyanide dissolution of gold nanorods before (1) and at different times after (2–11) cyanide addition. (b and c) TEM images of gold nanorods before and after cyanide treatment (0.5 mM CN^-), respectively. (d and e) TEM images of long gold nanorods before and after cyanide treatment. Adapted with permission from ref. [82]. © 2002 American Chemical Society.

liminary HRTEM results Sau and Murphy suggest the gold nanorods are single crystals possibly with {1 1 1} facets on the sides of the nanorods [86].

5. Reactivity and surface modification

We have seen in Section 2 that the most efficient protocols for the synthesis of gold nanorods are wet-chemical methods and involve the presence of surfactant molecules such as cetyltrimethylammonium bromide (C_{16}TAB), which function not only as rod-shape inducing agents, but also as capping agents. The presence of surfactant molecules on the surface of the gold nanorods strongly influences their reactivity and stability. In this section, we review reactivity and surface modification of gold nanorods, as well as some of the consequences of the change in chemical reactivity.

5.1. Anisotropic chemical reactivity

Murphy and co-workers studied the reactivity of gold spheroids and nanorods during cyanide dissolution and reaction with persulfate [82]. They have shown that in the presence of cyanide, the dissolution of short nanorods (aspect ratio 2–5) prepared in the presence of silver nitrate starts at the tips, while the width remains constant. Hence, reaction leads to lower aspect ratio nanorods and eventually to spheres that ultimately dissolve. Fig. 5.1 shows the time evolution of the UV–vis spectrum of gold nanorods in the presence of an excess of cyanide ions. It can be clearly seen that the longitudinal plasmon band progressively damps and blue-shifts with time (i.e., the aspect ratio of the nanorods decreases) up to a point where only the transverse plasmon band is present, indicating that the rod-shaped nanoparticles have been transformed into spheres, which was confirmed by TEM. A clear mechanism for the dissolution of the nanorods has not been provided.

A similar study was also performed for long nanorods prepared in the absence of silver nitrate [61]. Surprisingly, in this case the length of the nanorods did not decrease; instead, the dissolution occurred at various spots along the side edges (see Fig. 5.1d and e). Again, no mechanism for such an anomalous dissolution was proposed.

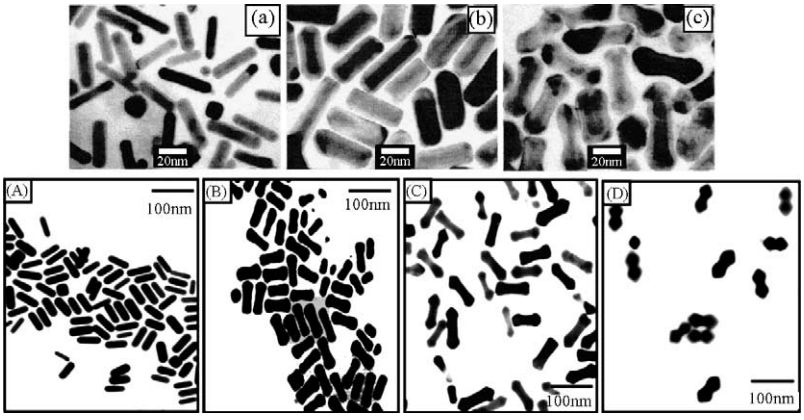

Fig. 5.2. Top: TEM of as prepared gold nanorods (a), Au@Ag core-shell nanorods with thin (b) and thick (c) silver layers, respectively. Reproduced with permission from ref. [103]. © 2001 American Chemical Society. Bottom: TEM of as prepared gold nanorods (A), and Au@Ag core-shell nanorods synthesized at pH 8.0 (B), 9.0 (C) and 10.0 (D). Reproduced with permission from ref. [106]. © 2004 American Chemical Society.

5.2. Au@Ag core-shell nanorods

Murphy and co-workers proposed a method to obtain pure silver nanorods and nanowires by a wet seed-mediated chemical method [102], in a similar way to that presented for gold nanorods. This protocol, while successful, marked an important step forward, but did not allow controlling the aspect ratio and monodispersity of the silver nanorods. As an alternative, Ah et al. proposed the deposition of silver onto previously synthesized monodisperse gold nanorods [103]. Silver deposition onto the surface of gold nanorods was carried out by reducing $AgCl_4^{3-}$ with hydroxylamine. The thickness of the deposited silver shell could be controlled simply by adjusting the concentration of the reactants. It is interesting to point out that whilst at low silver concentration the deposition was uniform, i.e., the obtained core-shell particles maintained a rod-like shape, when either the silver salt or reducing agent concentrations were increased, the final particles achieved a dumbbell shape arising from faster deposition of silver on the tips than on the side of the nanorods (see Fig. 5.2; top) [103]. The authors suggested that this effect could be related to the growth mechanism of gold nanorods in aqueous surfactant media, which agrees with later results [29].

More recently, Liu and Guyot-Sionnest presented a slightly different but simpler approach based on the reduction of silver nitrate onto the gold nanorod surface by ascorbic acid in the presence of C_{16}TAB and either citrate of PVP [104]. The core-shell nanorods obtained are similar to those reported by Ah et al. [103] but no clear reason for the use of citrate or PVP was provided. These authors simulated the spectra using a core-shell ellipsoid model within the dipole limit, and found they could adequately match theory to the experimental data [104]. They studied the reduction of the plasmon dephasing rate in core-shell nanorods and compared it with the values previously obtained for pure gold nanorods [105].

In a related work, Huang et al. studied the synthesis of Au@Ag core-shell nanorods in an aqueous surfactant solution under alkaline conditions (pH 8.0–10.0) [106]. Since the reduction of silver nitrate on the gold nanorod surface by ascorbic acid in aqueous surfactant media depends strongly on the pH of the solution [83,84,90,107], they used glycine buffers to control the pH of the growth solution. The silver coating was found to occur anisotropically in the presence of C_{16}TAB, and the final shape of the particles depended on the pH and silver concentration. As the pH of the solution was increased, the deposition rate of silver increased accordingly. These results demonstrated that the higher the pH, the higher the deposition rate at the tips compared to the sides, leading to the observed dumbbell shape (see Fig. 5.2; bottom). This effect can be explained in terms of either differential rates of crystal growth induced by the presence of C_{16}TAB [64,101] or an electrochemical mechanism that predicts a higher deposition rate at points of higher curvature [29].

5.3. Silica coating

The stability of C_{16}TAB-coated gold nanorod dispersions is high in aqueous solutions, but transfer into organic sol-

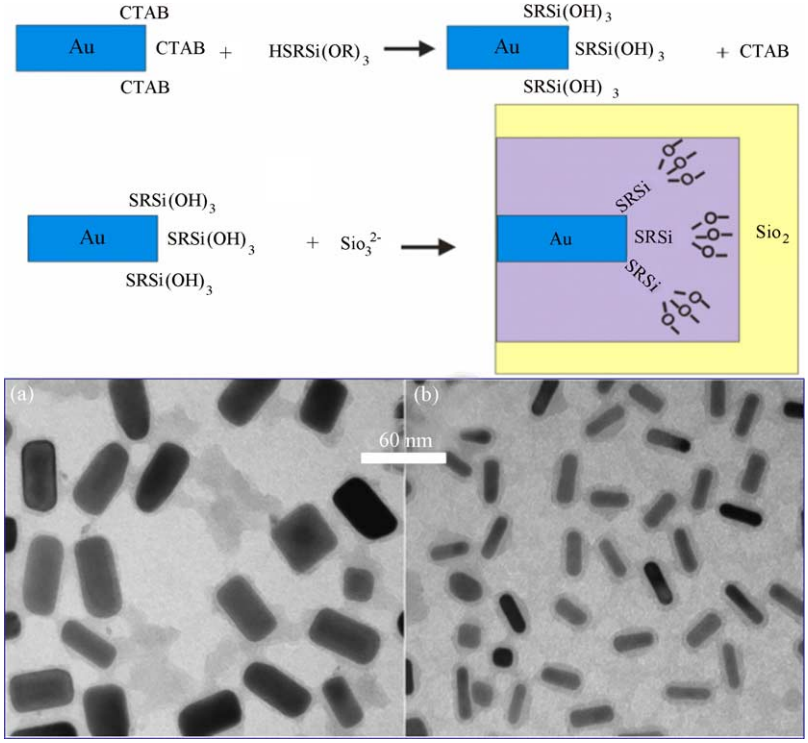

Fig. 5.3. Top: Scheme showing the steps required for silica coating of Au nanorods. Bottom: TEM of silica coated gold nanorods with different aspect ratios (a: 1.94; b: 3.08). Reproduced from ref. [85].

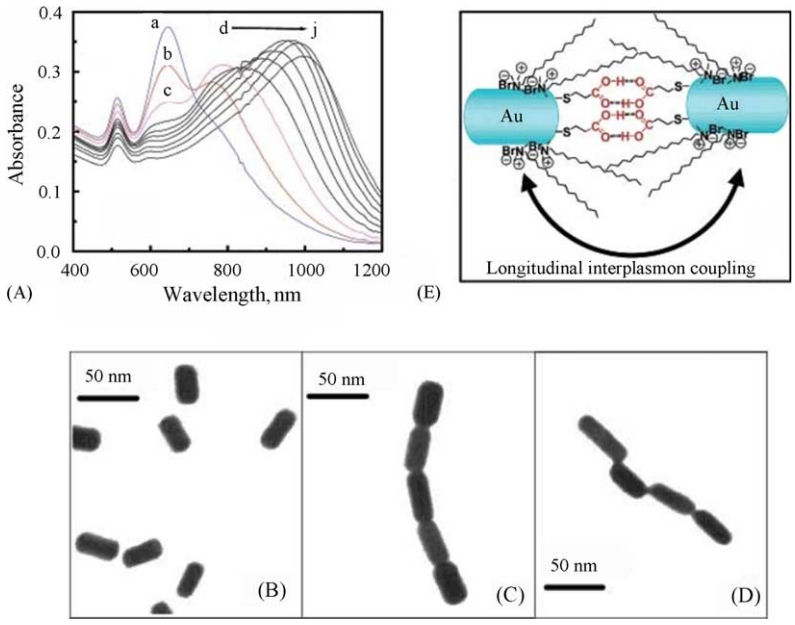

Fig. 5.4. (A) Time evolution (a–j) of the UV–vis spectra of gold nanorods in an acetonitrile–water mixture (4:1) after addition of 15 μM MPA. (B) TEM images of gold nanorods in the absence of MPA. (C) and (D) examples of linearly assembled gold nanorods in the presence of MPA. (E) Schematic representation of the intermolecular hydrogen bonding between MPA on adjacent nanorods. Adapted with permission from ref. [117]. © 2004 American Chemical Society.

vents is complicated, since the bilayer structure of the surfactant monomers on the gold nanorod surface makes the access of phase-transfer reagents to the surface difficult. Deposition of silica shells (silica coating) on gold nanorods has been proposed as a means to facilitate the manipulation of the gold nanorods, reducing aggregation and in addition preserving their optical properties. Various attempts have been presented in the literature, all of them using the protocol initially developed by Liz-Marzán et al. for the silica coating of citrate stabilized gold nanospheres [108,109]. In this method, a silane coupling agent is used as a surface modifier to enhance the affinity of gold for silica, which is then deposited from aqueous sodium silicate solution (Fig. 5.3). Wang and co-workers coated gold nanorods prepared by the electrochemical method and studied the influence of the silica shell on the shape transition induced by laser irradiation, finding a lower efficiency, i.e., more energy is required to produce a shape transition compared to surfactant stabilized nanorods, as might be expected from the rigidity of the silica matrix [49]. Murphy and co-workers adopted the same protocol for the silica coating of long gold nanorods prepared by the seed-mediated growth method, and subsequently used them as templates for the synthesis of hollow nanotubes through dissolution of the inner gold rods with cyanide [110]. Recently, Liz-Marzán's team coated short gold nanorods prepared by the seed-mediated method with silica (see Fig. 5.3) and studied their incorporation into nanostructures and nanocomposites [85,111], as discussed in Section 7 below.

5.4. Self-assembly of gold nanorods

The self-assembly of gold nanorods in aqueous C_{16}TAB solution was initially studied by El-Sayed and co-workers, who monitored the influence of nanoparticle concentration, solvent evaporation, ionic strength and surfactant concentration for gold nanorods with an aspect ratio of ∼4.6, prepared by the electrochemical method [66]. Depending on the conditions, the gold nanorods were observed to assemble in one, two- or three-dimensional structures. A similar study was carried out by Murphy and co-workers for longer nanorods (aspect ratio 13–18) prepared by the seed-mediated method [80]. They found similar results and indicated that surfactant-mediated interactions between gold nanorods of uniform size and shape lead to formation of liquid crystalline arrays in concentrated dispersions. Jana extended the study of nanoparticle self-assembly to other shapes, concluding that the nature of the self-assembly and its driving force depend on nanoparticle shape and also on the extent of shape anisotropy [79].

Wang and Kim studied the formation of one-dimensional nanostructures of rod-shape nanoparticles using the Langmuir–Blodgett technique, applied to thiol-capped gold nanorods. The different structures they observed were attributed to the different interactions between the structures as the surface pressure was varied [112–114].

Other reports about self-assembly of gold nanorods involve the cross-linking of nanorods through surface modification and chemical bonding. Dujardin et al. reported the specific organization of gold nanorods into anisotropic 3D-aggregates obtained by DNA hybridization. The key evidence for the biostructuring process was a "heating" analysis that clearly demonstrated its reversibility [115]. Murphy and co-workers showed that when C_{16}TAB-coated gold nanorods treated with biotin are mixed with streptavidin, a high proportion of end-to-end linked gold nanorods are formed [116]. Such directional assembly was initially attributed to the bi-

layer structure of the C_{16}TAB bound on the nanorod surface, such that the biotin preferentially bounds to the {1 1 1} faces at the ends of the rods [63,65].

Recently, Kamat and co-workers reported the longitudinal self-assembly of gold nanorods, associated with uniaxial plasmon coupling [117]. The assembly is carried out in acetonitrile–water mixtures and it is initiated and controlled by the presence of carboxylic acid derivatives (such as mercaptopropionic acid, MPA, and mercaptoundecanoic acid, MUA). These molecules present a thiol moiety that binds to the gold nanorod surface and a carboxyl moiety that assists the nanorod self-assembly through intermolecular hydrogen bonding. Upon addition of a carboxylic derivative the longitudinal plasmon band gradually shifts toward longer wavelengths (see Fig. 5.4). The spectral changes observed are explained on the basis of interplasmon coupling phenomena [9,118], suggesting that the gold nanorods organize linearly upon addition of MPA or MUA. This linear organization that allows uniaxial plasmon coupling has been demonstrated by TEM (Fig. 5.4C and D). The results are similar to those previously reported by Murphy and co-workers [116], furthermore implying that the C_{16}TAB monomers bound to the nanorod surface together with the added acetonitrile create a hydrophobic environment that promotes intermolecular dimerization (Fig. 5.4E) [117].

6. Gold nanorods and lasers

The interaction between metal or semiconductor nanoparticles and laser beams has been intensely studied during the last decade [49,119–136]. There are at least three distinct time regimes, which are important in metal nanoparticle laser studies. The irradiation of metal nanoparticles with a femtosecond pulse leads to a rapid increase in electron temperature. The resultant non-thermal electron distribution reaches equilibrium (internal electron thermalization) by elastic electron–electron collisions without releasing the absorbed photon energy within 100 fs, according to most calculations [137–139]. At this point, the non-equilibrium temperature difference between the electron gas and the lattice gives rise to energy exchange between the electrons and the lattice (electron–phonon coupling), so that heat is deposited into the lattice, leading to expansion within the timescale of the period of the phonon mode that correlates with the expansion coordinate. The laser energy therefore results in excitation of mechanical eigenmodes of the particles. The modes that can be excited can be calculated using continuum mechanism, and the frequency is a sensitive function of the particle geometry. The mechanical fluctuations of the particle ultimately transfer energy to the bath or medium around the particle in a period from 100 ps to 10 ns, depending on the particle size, the medium and the pulse energy. The transfer of energy to the bath depends on the thermal conductivity of particle and bath, the heat capacity of the two, and possibly on the solvent viscosity. At this point, the particle has recovered its ground state and has re-attained thermal equilibrium with the bath [140].

The above description, however, applies only to low laser pulse energies. For low energies, the ultrafast laser pulses raise the temperature of the nanoparticle lattice by only a few tens of degrees (depending on particle size and laser pump power). Under these conditions it will be possible to follow the electron–phonon coupling in real time using time-resolved techniques [140]. On the other hand, for high pump fluences the pulse energy can be powerful enough to raise the temperature of the metal above its melting point, and thereby it can be used as a convenient tool to control the shape and size distribution of nanoparticles [49,120–129,141]. As we shall see in this section, while femtosecond laser pulses can induce a shape transformation, such as a rod-to-sphere transition [141], nanosecond laser pulses can cause fragmentation into smaller particles [141]. The irradiation products not only depend on the laser flu-

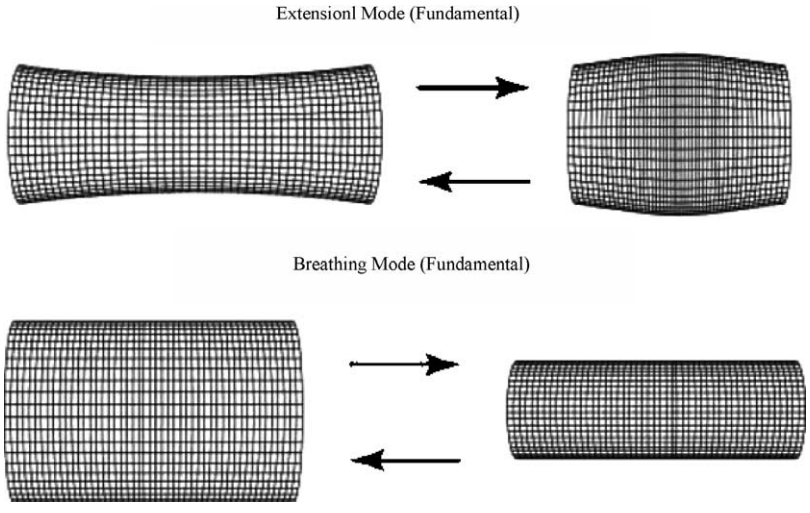

Fig. 6.1. Diagram showing the fundamental extensional and breathing modes of a cylindrical nanorod.

ence, but also on the excitation wavelength and laser pulse width.

We have divided this section into two parts, one devoted to ultrafast dynamics of gold nanorods, and the second to structural and morphological transitions.

6.1. Ultrafast dynamics of gold nanorods

Several groups have carried out detailed studies on the relaxation dynamics of excited electrons in spherical metal particles, comprised of gold [142–146], silver [147,148] or copper [149]. Fewer papers have been published on nanorod dynamics, and they are summarized here.

Combining experimental and theoretical studies, Hu et al. [150] established that laser-induced heating of cylindrical nanorods excites both the extensional and breathing modes of the rods. They calculated, using classical continuum mechanics, the temporal response of a cylindrical rod following excitation by a thermal pulse in the limit where the length of the rod greatly exceeds its radius. From symmetry considerations and assuming that the rod is composed of a linearly elastic isotropic material and remains at constant temperature after excitation (the thermal pulse has an infinitesimal time scale of duration), they showed that two modes dominated the mechanical response, though some 40–50 modes were identified with frequencies up to 10 times the fundamental eigenmode. These two dominant modes are the extensional mode and the breathing mode (see Fig. 6.1). The extensional mode consists of a combination of an axial expansion with a radial contraction and the breathing mode of a pure radial expansion and contraction. Thus, while the extensional mode probes the Young's modulus of the material, the breathing mode probes the bulk modulus.

Making these assumptions, Hu et al. established that the natural resonant frequencies of the extensional and breathing modes are given by the following respective equations:

$$\omega_{\text{ext}}^{(n)} = \frac{2n+1}{L}\pi\sqrt{\frac{E}{\rho}}, \tag{6.1}$$

$$\omega_{\text{br}}^{(n)} = \frac{\tau_n}{a}\sqrt{\frac{E(1-\upsilon)}{\rho(1+\upsilon)(1-2\upsilon)}} \tag{6.2}$$

where L and a are respectively the length and width of the rod, $n = 0, 1, 2, \ldots$ corresponds to the mode number, υ the Poisson's ratio of the rod, τ_n an eigenvalue, E is the Young's modulus and ρ is the density of the rod.

From these equations they also obtained:

$$\frac{\omega_{\text{br}}^{(0)}}{\omega_{\text{ext}}^{(0)}} = \frac{\tau_0}{\pi}\left(\frac{L}{a}\right)\sqrt{\frac{(1-\upsilon)}{(1+\upsilon)(1-2\upsilon)}} \tag{6.3}$$

which shows that the ratio of the resonant frequencies for the fundamental breathing and extensional modes can be directly measured from the temporal response following thermal excitation.

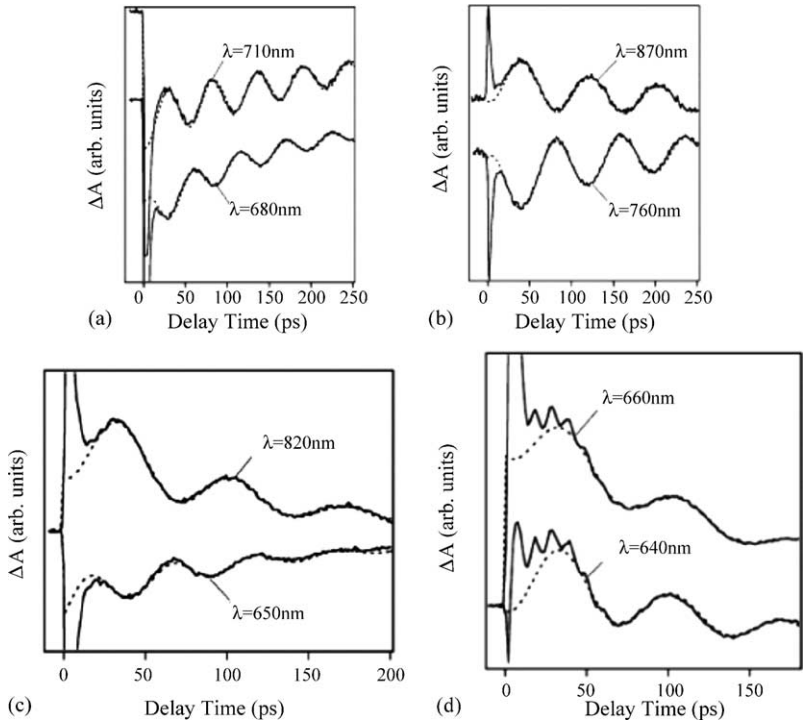

Fig. 6.2. Transient absorption traces for high quality (seed-mediated growth) samples with average lengths of (a) 46 ± 6 nm, (b) 75 ± 6 nm, and low quality samples with average lengths of (c) 42 ± 6 nm, (d) 55 ± 15 nm, for two different probe laser wavelengths. In all cases, the probe wavelengths presented lie on opposite sides of the longitudinal plasmon band of the sample. Reproduced with permission from ref. [150]. © 2003 American Chemical Society.

Experimentally, they carried out transient absorption experiments for gold nanorod samples with low and high monodispersity (prepared using the seed electrochemical technique and the mediated method, respectively). The average aspect ratios (length/width) of the rods varied between 2 and 6 and their length between 30 and 100 nm. The transient absorption experiments were performed with 400 nm pump laser pulses and the probe wavelengths were chosen to lie on either side of the longitudinal plasmon band of the sample. Fig. 6.2 shows transient absorption traces for the high quality samples for two different probe laser wavelengths. All traces present a fast component, which corresponds to electron–phonon coupling, and pronounced modulations with a period in the range of 40–120 ps, which was found to be similar for different probe wavelengths. Thus, the modulations are 180° out-of-phase for probe wavelengths on opposite sides of the longitudinal plasmon band, which was also observed for spherical particles [151]. However, different results were obtained when the same experiment was performed with low quality samples: the traces presented modulations with stronger damping, and the value of the period depended on the probe wavelength and the modulations were 60° out-of-phase. They claimed that these differences arise as a consequence of the polydispersity of the sample.

In some samples, a much faster modulation was observed, with a period of ca. 11 ps, as shown in Fig. 6.2d. This period was found to be approximately equal to the value for a vibrational motion corresponding to the radial expansion of the rod, that is, the breathing mode. Because the breathing mode is proportional to the width of the rod, the authors claimed that this mode would be more prominent for samples of thick rods. The same team calculated the period of the slower modulation at different probe wavelengths for all the samples analyzed above and found that, while the period for a given high quality sample was insensitive to the probe wavelength (Fig. 6.3a), the period for a low quality sample increased with increasing probe laser wavelength. In Fig. 6.3b, two curves are shown for samples with different widths. In this case, rods with the same aspect ratio have different periods for the same probe wavelength.

Good agreement was also found between the periods calculated experimentally and those calculated using Eq. (6.1) for the fundamental extensional vibrational mode (Fig. 6.4), which demonstrated that the dominant vibrational mode excited was the fundamental extensional mode.

From the experimental results, Hartland and co-workers calculated the Young's modulus of the nanorods and obtained a value of $E = 64 \pm 8$ MPa, which was substantially lower than the bulk value. This difference may reflect the fact that the extensional mode excited by the laser pulse probes the Young's modulus only along the growth direction, while the bulk gold modulus data is gleaned from polycrystalline samples [152,153]. However, more recently an analysis of the data shows that the lower value is inconsistent with any of the growth directions found from HRTEM studies. The authors now propose that the twinning plane along the major axis is responsible for the lower Young's modulus [154].

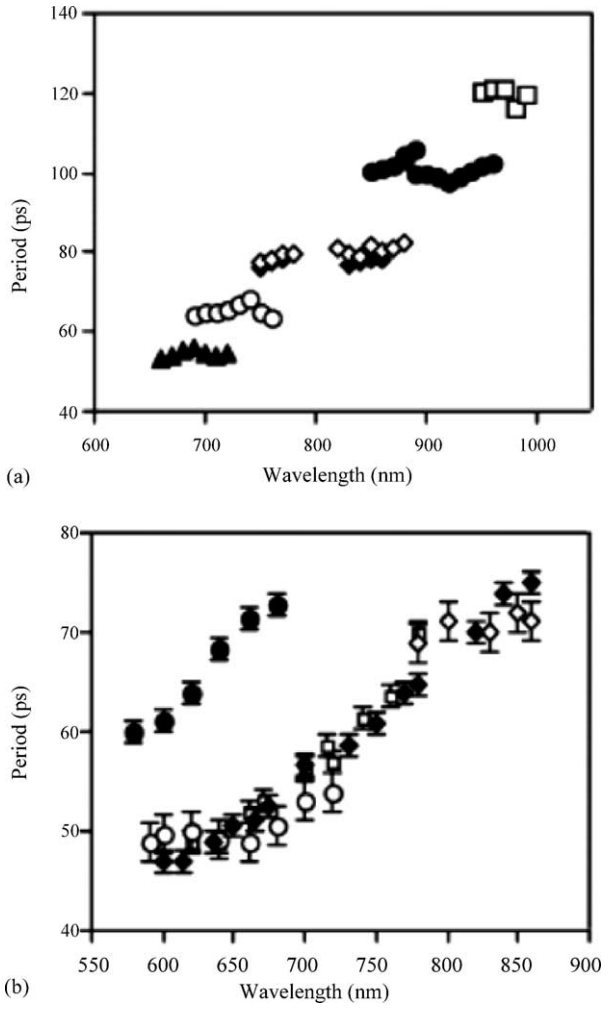

Fig. 6.3. Period vs. probe laser wavelength for different samples. (a) High quality samples. The different symbols indicate average lengths of (▲) 46 ± 6 nm, (◯) 61 ± 5 nm, (♦) 73 ± 4 nm, (◇) 75 ± 6 nm, (●) 89 ± 7 nm and (□) 108 ± 7. (b) Low quality samples. The different symbols indicate average lengths of (●) 55 ± 15 nm, (◯) 35 ± 10 nm, (□) 36 ± 10 nm, (♦) 42 ± 10 nm and (◇) 77 ± 20 nm. The error bars are contained within the symbol Note the different horizontal and vertical scales for each panel. Reproduced with permission from ref. [150]. © 2003 American Chemical Society.

Link et al. studied the transient-absorption dynamics of gold nanorods with an aspect ratio of 3.8 after excitation with 100-fs laser pump pulses at 400 nm [155,156]. They found that, the bleaching decays of the transverse and longitudinal plasmon adsorption bands resulted from electron–phonon and phonon–phonon relaxation processes and that both oscillations have similar electron dynamics (Fig. 6.5). Furthermore, they measured the plasmon bleach recovery for 15 and 48 nm spherical gold nanoparticles and found that the results are comparable to those obtained for the transverse and longitudinal modes of gold nanorods (Fig. 6.5). Therefore, they claimed that the relaxation dynamics appear to be independent of the shape of gold nanoparticles.

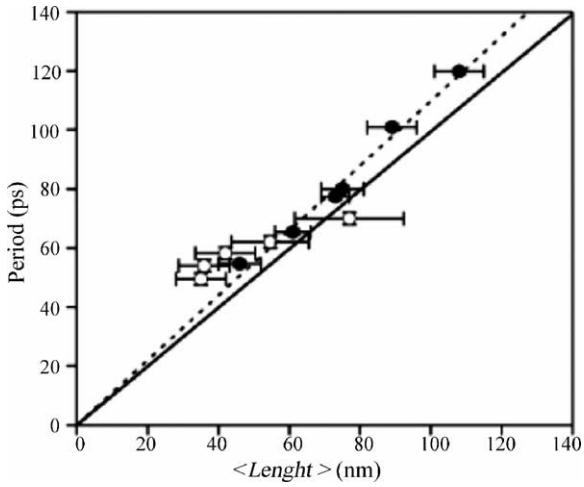

Fig. 6.4. Average period vs. average length for Au nanorods. The open symbols indicate the low quality samples, and the solid symbols show the high quality samples. The solid line is the calculated period for the fundamental extensional vibrational mode, Eq. (6.1). The dashed line represents a fit to the data assuming that the period is proportional to the length. The horizontal error bars reflect the polydispersity in the samples. Reproduced with permission from ref. [150]. © 2003 American Chemical Society.

6.2. Laser-induced structural and morphological transitions in gold nanorods

Several studies have revealed that irradiation with suitable laser pulses can induce size reduction of spherical particles by melting [120] or fragmentation [121,122]. However, spherical particles cannot undergo shape transformations, since the sphere is the most thermodynamically stable shape. During the last 5 years, different groups have reported that non-spherical particles can undergo irradiation-induced shape and size transformations [49,124]. We focus here on shape and size transitions of gold nanorods, synthesized using the electrochemical method described in Section 3.

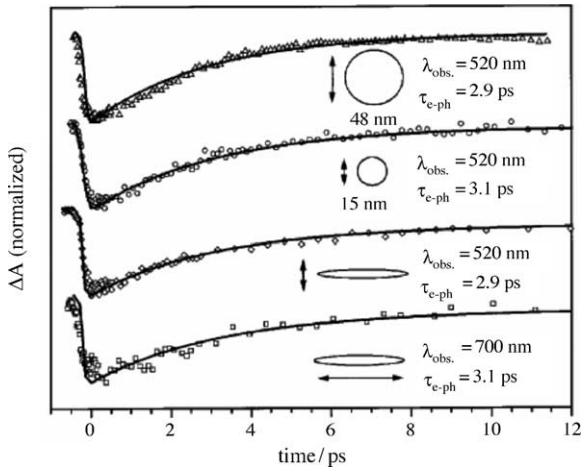

Fig. 6.5. Size and shape dependences of the electron–phonon relaxation time. Plasmon bleach recovery measured for 48 and 15 nm gold nanoparticles and for the transverse and longitudinal modes of gold nanorods with an average aspect ratio of 3.8 (top to bottom). The laser pump power and optical densities of the samples at the excitation wavelength were adjusted so that comparable initial electron temperatures were induced by the exciting femtosecond laser pulse. The results show that the measured electron–phonon relaxation times are independent of particle size and shape, eliminating the influence of electron-surface scattering as a dominant energy relaxation pathway. Reproduced with permission from ref. [156]. © 2000 Taylor and Francis.

The first paper published on this topic, which demonstrated the shape transition of gold nanorods into spheres, was authored by Chang et al. [49]. After irradiating an Au nanorod dispersion with a nanosecond laser tuned at 532 nm, they observed a decrease in intensity of the longitudinal plasmon, SP_{long}, band (indicating the disappearance of Au nanorods) and an enhancement of the band at ca.520 nm (increase of the Au nanosphere population), while the mean aspect ratio of the remaining nanorods remained roughly unchanged. This implied that the 532 nm irradiation induced the rod-to-sphere transformation through a photoannealing process. The authors claimed that by absorbing a 532 nm photon, the Au nanorod excited and accumulated phonon energy, which was responsible for its shape transition. However, exposure of the same nanorod sample to a nanosecond laser tuned to 1064 nm (SP_{long} of the nanorods) led to partial depletion and blue-shift of the SP_{long}band. This is consistent with a decrease in the mean aspect ratio of the rods and the formation of a new type of structures, Ø-shaped particles, which they considered to be a stable intermediate of the rod-to-sphere transition during the photoannealing process. These results are in agreement with those by Link et al. [157], which will be discussed below.

Almost at the same time, Link et al. reported on the photothermal stability of colloidal gold nanorods against laser irradiation with different pulse-widths [123,141,156]. They found that as the gold nanorod dispersion was irradiated with femtosecond laser pulses at 800 nm having pulse energies in the microJoule range, the nanorods melted selectively into nanodots with no fragmentation, as demonstrated by TEM images (Fig. 6.6b and d). They also showed that the average volume of the final irradiation product (exclusively spherical particles) was comparable to that of the starting nanorods. These researchers also monitored the melting process by optical absorption spectroscopy, finding a decrease in the intensity of the longitudinal plasmon band (due to the rod depletion) and an increase of the intensity of the transverse plasmon band (due to the higher extinction coefficient of the plasmon band of spherical particles) after successive intervals of laser irradiation.

However, when using nanoJoule pulses, selective melting of the nanorods strongly absorbing at the excitation wavelength was obtained, since only those absorb enough energy to undergo a shape transformation [123,141]. They observed an “optical hole” in the longitudinal plasmon band at the wavelength of the exciting laser pulse (Fig. 6.6e). Since this selective melting led to shorter but thicker rods (Fig. 6.6c) [6,7,26,27], this technique could be used to narrow down the initial size distribution of a gold nanorod sample.

Besides steady-state techniques, such as TEM and UV–vis absorption spectroscopy, Link et al. used time-resolved

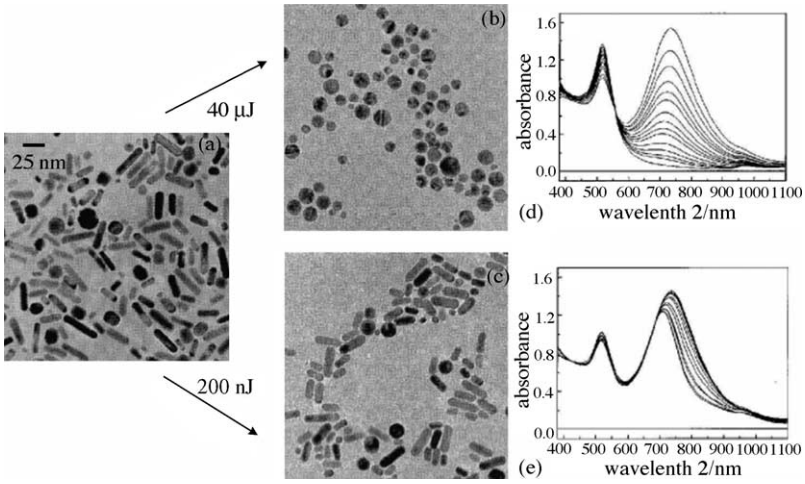

Fig. 6.6. Photothermal reshaping of gold nanorods with femtosecond laser pulses. (a) TEM image of the original gold nanorods solution having a mean aspect ratio of 3 ± 7. (b and c) TEM images of the same nanorod solution after irradiation with 100 fs laser pulses with pulse energies of 40 and 200 nJ respectively. The laser wavelength was 800 nm, which falls within the broad SP_{long} band. (d and e) Absorption spectra recorded after an increased irradiation time, so that the TEM image at the left corresponds to the last absorption spectrum measured. Reproduced with permission from ref. [156]. © 2000 Taylor and Francis.

pump–probe spectroscopy to measure the characteristic time for the conversion of gold nanorods into spheres [124], monitoring the disappearance rate of an appropriate longitudinal plasmon absorption. They calculated a shape transformation time of 30 ± 5 ps, which was independent of the laser pump power in the range of 5–20 μJ. Furthermore, the authors did not detect any clear dependence of the photoisomerization dynamics on the gold nanorod aspect ratio in the range 1.9–3.7 [124].

As expected, quite different results were obtained when a nanosecond rather than a femtosecond laser pulse was used [123,141,156], such that the energy threshold for the complete melting of the nanorods was reduced by a factor of 100 with femtosecond laser pulses [141,156]. It was also found that the irradiation of a sample with different laser pulse widths but the same laser pulse energy led to a complete melting of gold nanorods into spherical particles in the case of femtosecond laser pulses, but only partial melting in the case of nanosecond laser pulses, as confirmed the presence of Ø-shaped particles, as well as bent and twisted nanorods. These latter results were similar to those obtained after femtosecond irradiation at much lower pulse energies [123,156].

The initial postulate by Wang and co-workers [49] that the Ø-shaped particles correspond to an intermediate stage of the rod-to-sphere shape transformation [157] was demonstrated by Link et al. using HRTEM to monitor the structural changes undergone by gold nanorods after exposure to laser pulses (both nanosecond and femtosecond) with energies below the threshold required for complete melting. As described in Section 4, electrochemically synthesized gold nanorods with aspect ratios in the range 3–7 have {1 0 0}, {1 1 1} and {1 1 0} facets but no defects. Accordingly, no defects and {1 0 0}, {1 1 1} facets were found in the nanodots obtained via photothermal melting of such nanorods [89]. However, Link et al. [124,157] found that gold nanorods showed point and planar defects upon laser irradiation (Fig. 6.7a and b), which were assumed to constitute the precursors which initiated the steps that ultimately convert the relatively unstable {1 1 0} facets into more stable {1 0 0}, {1 1 1} facets [89]. A mechanism was proposed, which is schematically shown in Fig. 6.8, to explain the rod-to-sphere shape transformation. According to this mechanism, the shape transformation starts with the creation of point defects within the body of the particle (Fig. 6.8b) and whose local melting would give rise to

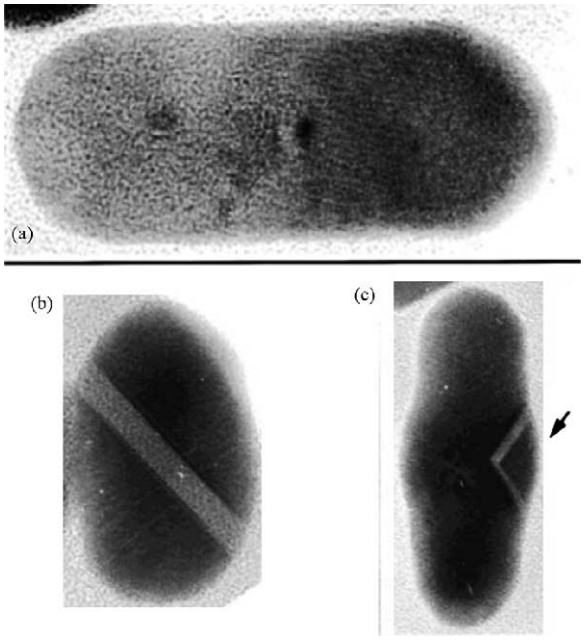

Fig. 6.7. HRTEM image of gold nanorods after exposure to femtosecond laser pulses (0.5 μJ per pulse) showing point defects (a) or twinned particles (b). (c) HRTEM image of a gold nanorod after exposure to nanosecond laser pulses (20 μJ per pulse) showing a twinned structure. Reproduced with permission from ref. [157]. © 2000 American Chemical Society.

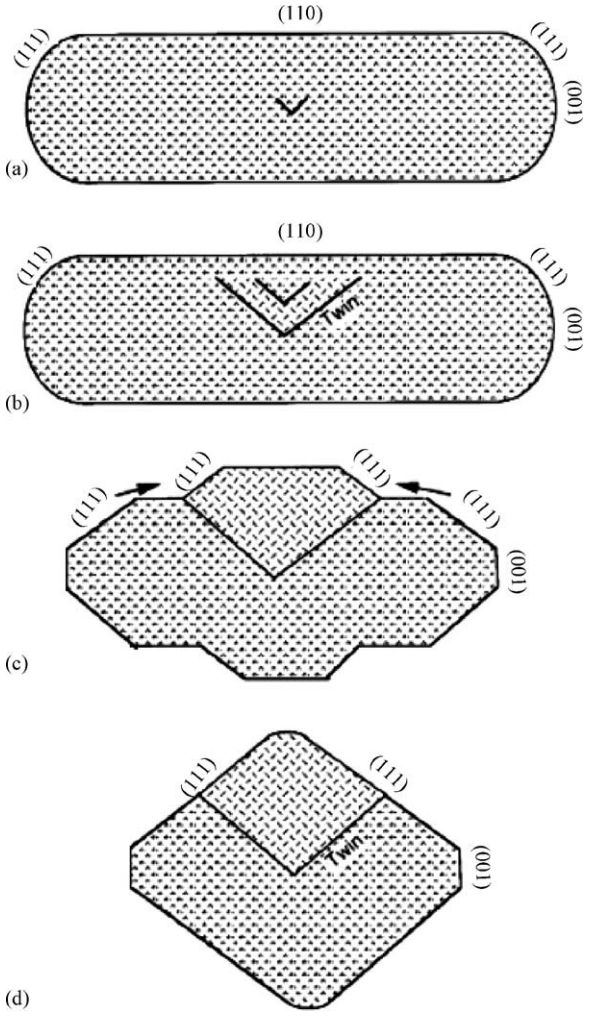

Fig. 6.8. Schematic process for the structural transformation from nanorods to nanodots. Reproduced with permission from ref. [157]. © 2000 American Chemical Society.

twins and stacking faults (Fig. 6.8c). Almost simultaneously, due to the lower stability of the {1 1 0} surface atoms, the surface melting starts, producing the growth of twinned crystals and eliminating the unstable surfaces (Fig. 6.8d).

El-Sayed and co-workers also tried to find a mechanism that explained the different effects produced in the gold nanorods with different laser pulse widths [123,156]. They proposed a mechanism whereby photon absorption (which heats the lattice and produces melting) and phonon-phonon relaxation (which drives heat loss from the lattice to the surroundings) are competitive processes. Melting occurs if the rate of heating of the lattice is faster than the rate of cooling. This mechanism can be summarized as follows:

$$(\mathrm{Au})_{\mathrm{NR}} \rightarrow [(\mathrm{Au})_{\mathrm{NR}}]^{\#}, \quad (6.4)$$

$$[(\mathrm{Au})_{\mathrm{NR}}]^{\#} \rightarrow [(\mathrm{Au})_{\mathrm{NR}}]^{\perp}, \quad (6.5)$$

$$[(\mathrm{Au})_{\mathrm{NR}}]^{\perp} \rightarrow [(\mathrm{Au})_{\mathrm{NR}}]^{\mathrm{vib}*} \quad (6.6)$$

$$[(\mathrm{Au})_{\mathrm{NR}}]^{\mathrm{vib}*} \rightarrow [(\mathrm{Au})_{\mathrm{NS}}], \quad (6.7)$$

$$[(\mathrm{Au})_{\mathrm{NP}}]^{\mathrm{vib}*} \rightarrow [(\mathrm{Au})_{\mathrm{NP}}]^{\mathrm{vib}**}, \quad (6.8)$$

$$[(\mathrm{Au})_{\mathrm{NP}}]^{\mathrm{vib}**} \rightarrow (\mathrm{Au})_{\mathrm{SNS}} \quad (6.9)$$

Processes (6.4)–(6.6) represent laser excitation and thermal heating of the electrons (less than 1 ps) [158] and lattice heating resulting from electron–phonon relaxation processes, respectively. NR, NS, NP and SNS stand for nanorods, nanospheres, nanoparticles and small nanospheres, respectively. In the case of femtosecond laser pulses, it was found that processes (6.5) and (6.6) were separated in time since the laser width (100 fs) was shorter than the electron–phonon relaxation time (1–3 ps) [142,143,148,159], but the laser intensity was so high that the lattice could be heated more efficiently and more rapidly than with a nanosecond laser pulse. However, with nanosecond laser pulses, the particles were bathed with light on a nanosecond time scale (process (6.8)), so that the molten or hot particles could still absorb additional photons (process (6.9)), which could lead to an increase in the lattice internal energy and to fragmentation of the particles [123].

Recently Wang et al. reported for the first time molecular dynamics simulations of the morphological and structural behavior of gold nanorods during continuous heating from 5 K to complete melting [160]. The simulated gold nanorods had the same aspect ratio, structure and geometry as the experimental rods but smaller sizes (10^3–10^4 atoms) due to computational limitations [123,141,157]. They found that the continuous heating of the gold nanorods induces a shape transition, which is accompanied by a structural change, and a melting transition. During the shape transition they also observed that rods became shorter and wider as observed experimentally by Link et al. (Fig. 6.8). A transition from fcc- into hcp-dominated structures was observed in some cases, depending on the calculation parameters (heating rate), but this remains to be confirmed experimentally. Eventually, it was observed that once the melting temperature was reached, the rods melted and the resulting disordered rods collapsed into the spherical shape.

7. Nanocomposites

A necessary intermediate step between the synthesis of metal nanoparticles and their use in practical devices is their organization within solid matrices, such as polymers or glasses/ceramics, which in turn can be processed into real devices. Such combinations of a solid matrix with nanosized components of a different material are often termed nanocomposites. Two main approaches have been followed for the preparation of nanocomposites comprising metal nanoparticles, involving either in situ formation of the nanoparticles or incorporation of pre-synthesized particles. As usual, both methods have their advantages and drawbacks. Formation of particles within the matrix is often simpler and just requires reduction of metal ions by thermal or photochemical methods

[161–163], but the control of particle size, composition, and shape of the formed nanoparticles is very difficult. On the other hand, pre-synthesized nanoparticles can be tailored by means of the various colloid chemistry techniques currently available, so that many more types of particles are possible, but surface modification is usually required to allow dispersion in the chosen matrix, so that aggregation during the processing stage (polymerization, sol–gel transition, etc.) can be obviated.

The first example comprises gels and glasses with optical functionalities, which are materials offering a number of technological applications, such as decorative coatings [164], catalysis [165], optical filters [166], non-linear optical materials [167], etc. Although most such composites to date have been comprised of spherical nanoparticles, the unusual optical properties of gold nanorods make their incorporation into these nanostructures very interesting. Although various techniques have been developed to dope glasses with metal nanoparticles by means of in situ reduction of metal salt precursors homogeneously distributed within the glass precursor [167], directional growth within a matrix is very complicated, and thus such techniques are rare. One possible exception is the electrochemical growth within porous membranes [35,44] described in Section 3, in which nanocomposites are formed prior to the dispersion of nanorods into solvents, but composite dimensions and control of interparticle spacing are strongly limited by the membranes used as templates.

A recent demonstration of the preparation of gold nanorods in silica, not only homogeneously dispersed, but also well aligned was published by Roorda et al. [168]. The method is based on high energy (tens of MeV) ion irradiation of gold–silica core-shell particles, which leads to an uniform deformation of both the gold cores and the silica shell [169]. The authors suggest that the deformation of the gold core is related to softening of the metal under the ion beam and a lateral stress imposed by the deformation of the silica shell, which suggests that a similar process performed on metal nanoparticles dispersed in a bulk silica gel or glass would not lead to uniform deformation. However, when ensembles of the starting core-shell colloids are irradiated, macroscopic composite materials with aligned nanorods can be obtained, as exemplified in Fig. 7.1. A certain degree of control over the aspect ratio can be achieved by varying the fluence of the ion beam, although very high energies can lead to further deformation into dumbbell-like structures [168].

The incorporation of preformed nanoparticles within gels and glasses has been reported for various systems [170] but often involves difficulties related to the homogeneous dispersion of individual nanoparticles, which is essential in the case of metal nanoparticles for optical applications, since otherwise changes in the optical response take place. Liz-Marzán and co-workers have recently reported a general procedure based on the coating of the precursor nanoparticles with silica, prior to sol–gel processing. Deposition of thin silica shells leads to an enhancement of the colloidal stability of metal nanoparticles in the sol–gel precursor solution, so that no aggregation takes place and silica gels and glasses are obtained which retain the optical properties of the nanoparticle dispersions. This method was initially applied to spherical metal nanoparticles, including Au [171] and AuAg alloys [172] but it could also be extended to gold nanorods of varying aspect ratio [85]. The spectra of the final nanocomposites only differ from those of the corresponding aqueous dispersions in a red-shift of the plasmon bands due to the increase in refractive index of the medium around the nanorods. A similar approach was also successfully applied to create organic–inorganic nanocomposites with tailored optical properties [111]. Such materials present superior mechanical properties, specially in terms of flexibility, but also a better transparency (lower light scattering) than standard silica gels [173]. Fig. 7.2 shows photographs of monoliths of ureasilicates [174,175] undoped and doped with gold and silver nanospheres, as well as gold nanorods of various aspect ratios, showing transparency, color uniformity and flexibility.

Related work has been recently reported for the preparation of large colloidal nanocomposites comprising gold nanoparticles and silica beads. Pastoriza-Santos et al. adapted the method proposed by Sadtler et al. for the electrostatically controlled deposition of gold nanospheres onto silica beads [176], to the coating of silica spheres with gold nanorods [177]. As shown in Fig. 7.3a, TEM revealed a random distribution of the rods on the silica surface, both before and after overcoating with a further silica shell. These onion-like particles do not suffer the problem of nanorods desorbing from the surface and are more chemically robust than simpler, rod-decorated silica carrier beads (Fig. 7.3b). UV–vis characterization of the composite colloids revealed that the position and intensity of the longitudinal plasmon bands of individual nanorods are retained in the micron-sized composite colloids and thus can be easily tailored throughout the visible and NIR [177].

The second large group of nanocomposites is formed by those where the host material is a polymer. Polymers offer

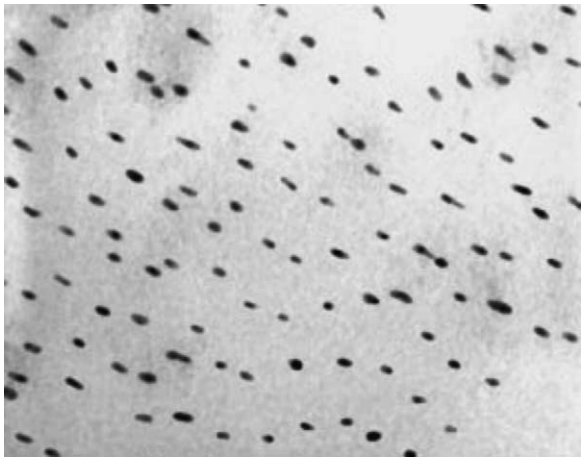

Fig. 7.1. TEM image of aligned Au nanorods observed after Se ion irradiation of an ensemble of closely packed core-shell colloids. Reproduced with permission from ref. [168]. © 2004 Wiley-VCH.

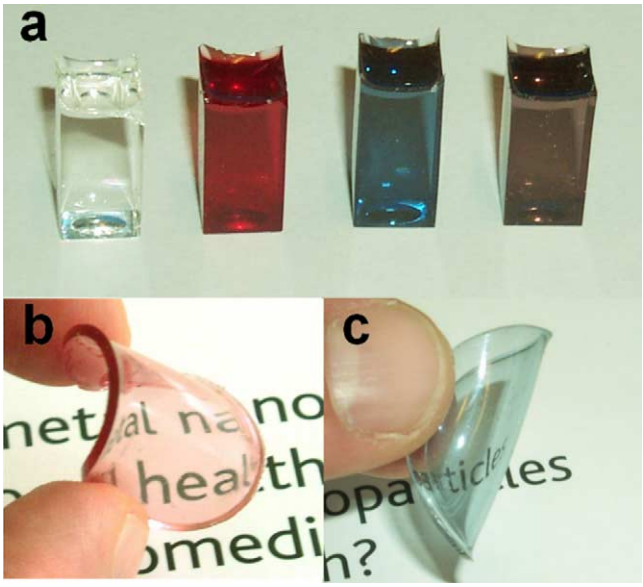

Fig. 7.2. (a) Photographs of monoliths made of (from left to right) undoped ureasil and ureasil doped with Au nanospheres, short and long nanorods. (b and c) Photographs of ureasil disk-shaped films doped with a low concentration of $Au@SiO_2$ nanospheres (b) and short nanorods (c). Reproduced with permission from ref. [111]. © 2004 American Chemical Society.

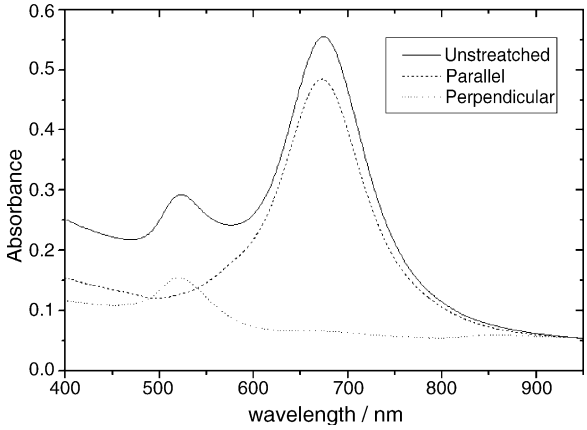

Fig. 7.4. UV–vis spectra of an Au nanorod-PVA film under non-polarized light, showing two plasmon bands, and under parallel and perpendicular polarized light (with respect to the longitudinal axis of the film).

further possibilities for processing, which are important in the case of nanorods, since procedures for controlled alignment would be extremely useful, for they would allow to fabricate materials with polarization-dependent optical properties. A preliminary work related to such composite materials was published by Dirix et al. [178] using polyethylene films containing silver nanoparticles. The films were drawn in a hot shoe, leading to alignment of nanoparticle aggregates, which showed polarization-dependent optical response. A more refined procedure was used by van der Zande et al., who prepared thin films of gold nanorods (template method) dispersed in poly(vinyl alcohol) (PVA) by simply drying a colloid in the presence of dissolved PVA [179]. Initially, the optical properties of the prepared films resembled those of the gold nanorod dispersion, displaying both longitudinal and transversal plasmon resonances, since the nanoparticles were randomly distributed within the film. Alignment of the gold nanorods in a preferred direction was achieved by warming up and stretching the composite film [180,181]. They analyzed the extent of elongation needed for the alignment of the gold nanorods, as well as the optical properties of fully aligned nanorods within the films as a function of the polarization angle, and found a strong dependence of the absorbance on the polarization angle. This procedure works very well, as shown in Fig. 7.4. As expected, the spectrum of an unstretched composite Au–PVA film displays two resonance peaks corresponding to the transverse and longitudinal plasmon bands, and the same result is observed in the case of a stretched film under non-polarized light, since it contains all orientations of the oscillating electric field. However, when the spectrum is measured under light polarized parallel to the stretching direction of the film, the longitudinal plasmon band is selectively excited, while under light polarized perpendicular to the stretching direction, only the transverse coupling is observed [179]. The gradual alignment of the nanorods within the films with increasing elongation can be demonstrated by confocal scanning laser microscopy, as well as by TEM [179]. The limitation of this nanocomposite system re-

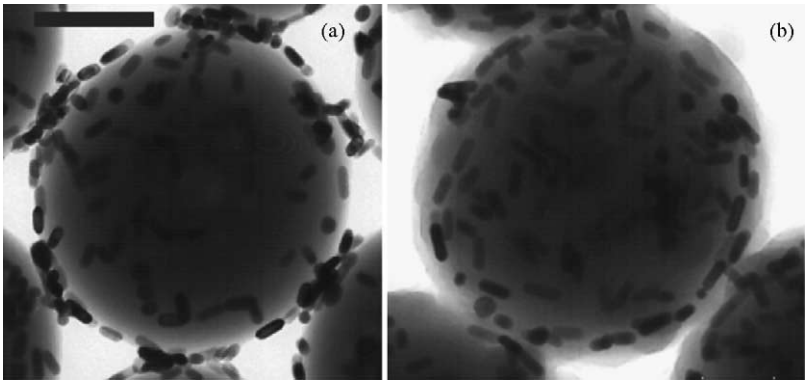

Fig. 7.3. TEM images of gold nanorod-coated silica particles (270 nm) before (a) and after further growth with silica. The outer shell thickness is about 30 nm. The scale bar is 100 nm.

sides in the fact that alignment is not reversible, which could be achieved if flexible polymers were used as substrates.

8. Applications

Since the synthesis of gold nanorods in decent yield and monodispersity has been developed comparatively recently, only a few papers have been published related to their applications, but great possibilities have been pointed out. Meyer and co-workers have recently reviewed the biological applications of high aspect ratio nanoparticles, mainly including those related to gold nanorods and nanotubes, developed by Martin and co-workers [182]. Specially interesting are their works related to chemical separation and sensing using gold nanotube membranes, through the control of pore size of the nanotubes as well as their surface modification [183,184].

Other applications are directly related to the optical properties of the nanorods. For example, the sensitivity of the plasmon resonance frequency toward the refractive index of the surroundings makes them suitable candidates for biological sensing applications [185]. On the other hand, the polarization-dependent response can be extremely useful in applications such as displays or encoding security systems [178]. A further refinement of this type of applications is related to the thermal sensitivity of the nanorods (see Section 6.2). Wilson et al. have demonstrated [32] that both oriented and non-oriented silver nanorods can be selectively melted within PVA thin films by simply irradiating with a single pulse of a ns laser, leading to reshaping into spheres and a consequent color change in the film. Since the optical response of the spheres is insensitive to the polarization of light, the result is selective patterning (or writing). Recent results show that laser writing can also be readily applicable to PVA films containing gold nanorods of various aspect ratios, and thus expanding the possibilities for practical applications of such films [186]. Further applications related to the nonlinear optical response of the nanorods can also be envisaged, but still need to be developed.

Acknowledgements

Financial support from the Spanish Xunta de Galicia (Project No. PGIDIT03TMT30101PR) and Ministerio de Educación y Ciencia/FEDER (Project MAT2004-02991) are gratefully acknowledged.

References

[1] U. Kreibig, J. Phys. F: Met. Phys. 4 (1974) 999.
[2] U. Kreibig, Z. Phys. 31 (1978) 39.
[3] U. Kreibig, Handbook Opt. Properties 2 (1997) 145.
[4] U. Kreibig, L. Genzel, Surf. Sci. 156 (1985) 678.
[5] H.C. van der Hulst, Light Scattering by Small Particles, John Wiley and Sons, New York, 1957.
[6] M. Kerker, The Scattering of Light and Other Electromagnetic Radiation, Academic Press, New York, 1969.
[7] C.F. Bohren, D.R. Huffman, Absorption and Scattering of Light by Small Particles, Wiley, New York, 1983.
[8] N. Felidj, J. Aubard, G. Levi, J. Chem. Phys. 111 (1999) 1195.
[9] K.L. Kelly, E. Coronado, L.L. Zhao, G.C. Schatz, J. Phys. Chem. B 107 (2003) 668.
[10] E.D. Purcell, C.R. Pennypacker, Astrophys. J. 186 (1973) 705.
[11] B.T. Draine, P.J. Flatau, J. Opt. Soc. Am. A 11 (1994) 1491.
[12] W.-H. Yang, G.C. Schatz, R.P. Van Duyne, J. Chem. Phys. 103 (1995) 869.
[13] L. Genzel, T.P. Martin, U. Kreibig, Z. Phys. 21 (1975) 339.
[14] G. Mie, Ann. Phys. 25 (1908) 377.
[15] E.D. Palik (Ed.), Handbook of Optical Constants of Solids, Academic Press, Orlando, 1985.
[16] R. Gans, Ann. Phys. 37 (1912) 881.
[17] R. Ruppin, J. Opt. Soc. Am. B 6 (1989) 1559.
[18] R. Ruppin, J. Phys. D 23 (1990) 757.
[19] R. Fuchs, Phys. Rev. B 11 (1975) 1732.
[20] N.A.F. Al-Rawashdeh, M.L. Sandrock, C.J. Seugling, C.A. Foss Jr., J. Phys. Chem. B 102 (1998) 361.
[21] R. Ruppin, J. Phys.: Condens. Matter 10 (1998) 7869.
[22] B.T. Draine, J.J. Goodman, Astrophys. J. 405 (1993) 685.
[23] B.T. Draine, P.J. Flatau, Program DDSCAT. Scripps Institute of Oceanography, University of California, San Diego, CA.
[24] S.D. Stookey, R.J. Araujo, Appl. Opt. 7 (1968) 777.
[25] C.A. Foss Jr., G.L. Hornyak, J.A. Stockert, C.R. Martin, J. Phys. Chem. 98 (1994) 2963.
[26] Y.-Y. Yu, S.-S. Chang, C.-L. Lee, C.R.C. Wang, J. Phys. Chem. B 101 (1997) 6661.
[27] S. Link, M.B. Mohamed, M.A. El-Sayed, J. Phys. Chem. B 103 (1999) 3073.
[28] B.M.I. van der Zande, M.R. Boehmer, L.G.J. Fokkink, C. Schoenenberger, Langmuir 16 (2000) 451.
[29] J. Pérez-Juste, L.M. Liz-Marzán, S. Carnie, D.Y.C. Chan, P. Mulvaney, Adv. Funct. Mater. 14 (2004) 571.
[30] B. Yan, Y. Yang, Y. Wang, J. Phys. Chem. B 107 (2003) 9159.
[31] J.H. Weaver, C. Krafka, D.W. Lynch, E.E. Koch (Eds.). Optical Properties of Metals. Physics Data Series, Fachinformationszentrum, Karlsruhe, 1981.
[32] O. Wilson, G.J. Wilson, P. Mulvaney, Adv. Mater. 14 (2002) 1000.
[33] C.A. Foss Jr., G.L. Hornyak, J.A. Stockert, C.R. Martin, J. Phys. Chem. 96 (1992) 7497.
[34] C.R. Martin, Science 266 (1994) 1961.
[35] C.R. Martin, Chem. Mater. 8 (1996) 1739.
[36] C.A. Foss Jr., G.L. Hornyak, J.A. Stockert, C.R. Martin, Adv. Mater. 5 (1993) 135.
[37] R.M. Penner, C.R. Martin, Anal. Chem. 59 (1987) 2625.
[38] B.M.I. van der Zande, M.R. Boehmer, L.G.J. Fokkink, C. Schoenenberger, J. Phys. Chem. B 101 (1997) 852.
[39] V.M. Cepak, C.R. Martin, J. Phys. Chem. B 102 (1998) 9985.
[40] J.C. Hulteen, C.R. Martin, J. Mater. Chem. 7 (1997) 1075.
[41] K.B. Jirage, J.C. Hulteen, C.R. Martin, Science 278 (1997) 655.
[42] C. Schoenenberger, B.M.I. van der Zande, L.G.J. Fokkink, M. Henny, C. Schmid, M. Krueger, A. Bachtold, R. Huber, H. Birk, U. Staufer, J. Phys. Chem. B 101 (1997) 5497.
[43] Z. Hou, N.L. Abbott, P. Stroeve, Langmuir 16 (2000) 2401.
[44] M. Wirtz, C.R. Martin, Adv. Mater. 15 (2003) 455.
[45] V.M. Cepak, J.C. Hulteen, G. Che, K.B. Jirage, B.B. Lakshmi, E.R. Fisher, C.R. Martin, H. Yoneyama, Chem. Mater. 9 (1997) 1065.
[46] V.M. Cepak, J.C. Hulteen, G. Che, K.B. Jirage, B.B. Lakshmi, E.R. Fisher, C.R. Martin, J. Mater. Res. 13 (1998) 3070.
[47] Y. Sun, B. Wiley, Z.-Y. Li, Y. Xia, J. Am. Chem. Soc. 126 (2004) 9399.
[48] Y. Sun, Y. Xia, Adv. Mater. 16 (2004) 264.
[49] S.-S. Chang, C.-W. Shih, C.-D. Chen, W.-C. Lai, C.R.C. Wang, Langmuir 15 (1999) 701.

[50] M.T. Reetz, W. Helbig, J. Am. Chem. Soc. 116 (1994) 7401.
[51] M. Toernblom, U. Henriksson, J. Phys. Chem. B 101 (1997) 6028.
[52] P. Mulvaney, M. Giersig, A. Henglein, J. Phys. Chem. 97 (1993) 7061.
[53] A. Henglein, M. Giersig, J. Phys. Chem. 98 (1994) 6931.
[54] K.R. Brown, M.J. Natan, Langmuir 14 (1998) 726.
[55] K.R. Brown, D.G. Walter, M.J. Natan, Chem. Mater. 12 (2000) 306.
[56] K.R. Brown, L.A. Lyon, A.P. Fox, B.D. Reiss, M.J. Natan, Chem. Mater. 12 (2000) 314.
[57] N.R. Jana, L. Gearheart, C.J. Murphy, Chem. Mater. 13 (2001) 2313.
[58] M.A. Watzky, R.G. Finke, J. Am. Chem. Soc. 119 (1997) 10382.
[59] N.R. Jana, L. Gearheart, C.J. Murphy, Langmuir 17 (2001) 6782.
[60] A. Henglein, M. Giersig, J. Phys. Chem. B 103 (1999) 9533.
[61] N.R. Jana, L. Gearheart, C.J. Murphy, J. Phys. Chem. B 105 (2001) 4065.
[62] B.D. Busbee, S.O. Obare, C.J. Murphy, Adv. Mater. 15 (2003) 414.
[63] B. Nikoobakht, M.A. El-Sayed, Langmuir 17 (2001) 6368.
[64] C.J. Johnson, E. Dujardin, S.A. Davis, C.J. Murphy, S. Mann, J. Mater. Chem. 12 (2002) 1765.
[65] J. Gao, C.M. Bender, C.J. Murphy, Langmuir 19 (2003) 9065.
[66] B. Nikoobakht, Z.L. Wang, M.A. El-Sayed, J. Phys. Chem. B 104 (2000) 8635.
[67] K. Torigoe, K. Esumi, Langmuir 8 (1992) 59.
[68] J. Pérez-Juste et al., manuscript in preparation.
[69] A. Henglein, D. Meisel, Langmuir 14 (1998) 7392.
[70] S. Biggs, P. Mulvaney, J. Chem. Phys. 100 (1994) 8501.
[71] A. Taleb, C. Petit, M.P. Pileni, Chem. Mater. 9 (1997) 950.
[72] H. Yao, O. Momozawa, T. Hamatani, K. Kimura, Chem. Mater. 13 (2001) 4692.
[73] G.-T. Wei, F.-K. Liu, C.R.C. Wang, Anal. Chem. 71 (1999) 2085.
[74] N.R. Jana, Chem. Commun. (2003) 1950.
[75] L. Onsager, Ann. N. Y. Acad. Sci. 51 (1949) 627.
[76] M. Adams, Z. Dogic, S.L. Keller, S. Fraden, Nature 393 (1998) 349.
[77] F.M. van der Kooij, H.N.W. Lekkerkerker, Langmuir 16 (2000) 10144.
[78] F.M. van der Kooij, D. van der Beek, H.N.W. Lekkerkerker, J. Phys. Chem. B 105 (2001) 1696.
[79] N.R. Jana, Angew. Chem., Int. Ed. Engl. 43 (2004) 1536.
[80] N.R. Jana, L.A. Gearheart, S.O. Obare, C.J. Johnson, K.J. Edler, S. Mann, C.J. Murphy, J. Mater. Chem. 12 (2002) 2909.
[81] N.R. Jana, L. Gearheart, C.J. Murphy, Adv. Mater. 13 (2001) 1389.
[82] N.R. Jana, L. Gearheart, S.O. Obare, C.J. Murphy, Langmuir 18 (2002) 922.
[83] T. Pal, S. De, N.R. Jana, N. Pradhan, R. Mandal, A. Pal, A.E. Beezer, J.C. Mitchell, Langmuir 14 (1998) 4724.
[84] B. Nikoobakht, M.A. El-Sayed, Chem. Mater. 15 (2003) 1957.
[85] J. Pérez-Juste, M.A. Correa-Duarte, L.M. Liz-Marzán, Appl. Surf. Sci. 226 (2004) 137.
[86] T.K. Sau, C.J. Murphy, Langmuir 20 (2004) 6414.
[87] A.P. Alivisatos, J. Phys. Chem. 100 (1996) 13226.
[88] Z.L. Wang, R.P. Gao, B. Nikoobakht, M.A. El-Sayed, J. Phys. Chem. B 104 (2000) 5417.
[89] Z.L. Wang, M.B. Mohamed, S. Link, M.A. El-Sayed, Surf. Sci. 440 (1999) 809.
[90] F. Kim, J.H. Song, P. Yang, J. Am. Chem. Soc. 124 (2002) 14316.
[91] K. Esumi, J. Hara, N. Aihara, K. Usui, K. Torigoe, J. Colloid Interface Sci. 208 (1998) 578.
[92] E. Leontidis, K. Kleitou, T. Kyprianidou-Leodidou, V. Bekiari, P. Lianos, Langmuir 18 (2002) 3659.
[93] Y. Niidome, K. Nishioka, H. Kawasaki, S. Yamada, Chem. Commun. (2003) 2376.
[94] N. Taub, O. Krichevski, G. Markovich, J. Phys. Chem. B 107 (2003) 11579.
[95] Z. Wei, A.J. Mieszawska, F.P. Zamborini, Langmuir 20 (2004) 4322.
[96] Z.L. Wang, J. Phys. Chem. B 104 (2000) 1153.
[97] P.L. Gai, K. Kourtakis, Science 267 (1995) 661.
[98] E.D. Boyes, P.L. Gai, Ultramicroscopy 67 (1997) 219.
[99] P.L. Gai, Adv. Mater. 10 (1998) 1259.
[100] P.L. Gai, Microsc. Microanal. 8 (2002) 21.
[101] P.L. Gai, M.A. Harmer, Nano Lett. 2 (2002) 771.
[102] N.R. Jana, L. Gearheart, C.J. Murphy, Chem. Comm. (2001) 617.
[103] C.S. Ah, S.D. Hong, D.-J. Jang, J. Phys. Chem. B 105 (2001) 7871.
[104] M. Liu, P. Guyot-Sionnest, J. Phys. Chem. B 108 (2004) 5882.
[105] C. Sonnichsen, T. Franzl, T. Wilk, G. von Plessen, J. Feldmann, O. Wilson, P. Mulvaney, Phys. Rev. Lett. 88 (2002), 077402/1.
[106] C.-C. Huang, Z. Yang, H.-T. Chang, Langmuir 20 (2004) 6089.
[107] J.H. Hodak, A. Henglein, M. Giersig, G.V. Hartland, J. Phys. Chem. B 104 (2000) 11708.
[108] L.M. Liz-Marzán, M. Giersig, P. Mulvaney, Chem. Commun. (1996) 731.
[109] L.M. Liz-Marzán, M. Giersig, P. Mulvaney, Langmuir 12 (1996) 4329.
[110] S.O. Obare, N.R. Jana, C.J. Murphy, Nano Lett. 1 (2001) 601.
[111] V.I. Boev, J. Pérez-Juste, I. Pastoriza-Santos, C.J.R. Silva, M. de Gomes, L.M. Liz-Marzán, Langmuir 20 (2004) 10268.
[112] S. Kwan, F. Kim, J. Akana, P. Yang, Chem. Commun. (2001) 447.
[113] F. Kim, S. Kwan, J. Akana, P. Yang, J. Am. Chem. Soc. 123 (2001) 4360.
[114] P. Yang, F. Kim, Chem. Phys. Chem. 3 (2002) 503.
[115] E. Dujardin, S. Mann, L.-B. Hsin, C.R.C. Wang, Chem. Commun. (2001) 1264.
[116] K.K. Caswell, J.N. Wilson, U.H.F. Bunz, C.J. Murphy, J. Am. Chem. Soc. 125 (2003) 13914.
[117] K.G. Thomas, S. Barazzouk, B.I. Ipe, S.T.S. Joseph, P.V. Kamat, J. Phys. Chem. B 108 (2004) 13066.
[118] N. Felidj, J. Aubard, G. Levi, J.R. Krenn, G. Schider, A. Leitner, F.R. Aussenegg, Phys. Rev. B 66 (2002), 245407/1.
[119] J.Z. Zhang, Acc. Chem. Res. 30 (1997) 423.
[120] A.L. Stepanov, D.E. Hole, A.A. Bukharaev, P.D. Townsend, N.I. Nurgazizov, Appl. Surf. Sci. 136 (1998) 298.
[121] P.V. Kamat, M. Flumiani, G.V. Hartland, J. Phys. Chem. B 102 (1998) 3123.
[122] H. Kurita, A. Takami, S. Koda, Appl. Phys. Lett. 72 (1998) 789.
[123] S. Link, C. Burda, M.B. Mohamed, B. Nikoobakht, M.A. El-Sayed, J. Phys. Chem. A 103 (1999) 1165.
[124] S. Link, C. Burda, B. Nikoobakht, M.A. El-Sayed, Chem. Phys. Lett. 315 (1999) 12.
[125] A. Takami, H. Kurita, S. Koda, J. Phys. Chem. B 103 (1999) 1226.
[126] H. Fujiwara, S. Yanagida, P.V. Kamat, J. Phys. Chem. B 103 (1999) 2589.
[127] M. Kaempfe, T. Rainer, K.J. Berg, G. Seifert, H. Graener, Appl. Phys. Lett. 74 (1999) 1200.
[128] T. Wenzel, J. Bosbach, A. Goldmann, F. Stietz, F. Trager, Appl. Phys. B 69 (1999) 513.
[129] J. Bosbach, D. Martin, F. Stietz, T. Wenzel, F. Trager, Appl. Phys. Lett. 74 (1999) 2605.
[130] S. Link, M.A. El-Sayed, J. Phys. Chem. B 103 (1999) 8410.
[131] J.H. Hodak, A. Henglein, G.V. Hartland, J. Phys. Chem. B 104 (2000) 9954.
[132] J.Y. Bigot, V. Halte, J.C. Merle, A. Daunois, Chem. Phys. 251 (2000) 181.
[133] N. Del Fatti, F. Vallee, C. Flytzanis, Y. Hamanaka, A. Nakamura, Chem. Phys. 251 (2000) 215.
[134] S. Stagira, M. Nisoli, S. De Silvestri, A. Stella, P. Tognini, P. Cheyssac, R. Kofman, Chem. Phys. 251 (2000) 259.
[135] C. Voisin, N. Del Fatti, D. Christofilos, F. Vallee, J. Phys. Chem. B 105 (2001) 2264.
[136] M.A. El-Sayed, Acc. Chem. Res. 34 (2001) 257.

[137] C.K. Sun, F. Vallee, L. Acioli, E.P. Ippen, J.G. Fujimoto, Phys. Rev. B 48 (1993) 12365.
[138] C.K. Sun, F. Vallee, L.H. Acioli, E.P. Ippen, J.G. Fujimoto, Phys. Rev. B 50 (1994) 15337.
[139] G.V. Hartland, Phys. Chem. Chem. Phys. 6 (2004) 5263.
[140] M. Hu, G.V. Hartland, in: L.M. Liz-Marzán, P.V. Kamat (Eds.), Nanoscale Materials, Kluwer, Boston, 2003, p. 97.
[141] S. Link, C. Burda, B. Nikoobakht, M.A. El-Sayed, J. Phys. Chem. B 104 (2000) 6152.
[142] T.S. Ahmadi, S.L. Logunov, M.A. El-Sayed, J. Phys. Chem. 100 (1996) 8053.
[143] M. Perner, P. Bost, U. Lemmer, G. von Plessen, J. Feldmann, U. Becker, M. Menning, M. Schmitt, H. Schmidt, Phys. Rev. Lett. 78 (1997) 2192.
[144] B.A. Smith, D.M. Waters, A.E. Faulhaber, M.A. Kreger, T.W. Roberti, J.Z. Zhang, J. Sol–Gel Sci. Tech. 9 (1997) 125.
[145] B.A. Smith, J.Z. Zhang, U. Giebel, G. Schmid, Chem. Phys. Lett. 270 (1997) 139.
[146] H. Inouye, K. Tanaka, I. Tanahashi, K. Hirao, Phys. Rev. B 57 (1998) 11334.
[147] T.W. Roberti, B.A. Smith, J.Z. Zhang, J. Chem. Phys. 102 (1995) 3860.
[148] J.H. Hodak, I. Martini, G.V. Hartland, J. Phys. Chem. B 102 (1998) 6958.
[149] T. Tokizaki, A. Nakamura, S. Kaneko, K. Uchida, S. Omi, H. Tanji, Y. Asahara, Appl. Phys. Lett. 65 (1994) 941.
[150] M. Hu, X. Wang, G.V. Hartland, P. Mulvaney, J. Pérez Juste, J.E. Sader, J. Am. Chem. Soc. 125 (2003) 14925.
[151] G.V. Hartland, J. Chem. Phys. 116 (2002) 8048.
[152] L.D. Landau, E.M. Lifshitz, Theory of Elasticity, Pergamon Press, Oxford, 1970.
[153] G. Simmons, H. Wang, Single-Crystal Elastic Constants and Calculated Aggregate Properties: a Handbook, The MIT Press, Cambridge, 1971.
[154] M. Hu, P. Hillyard, G.V. Hartland, T. Kosel, J. Pérez Juste, P. Mulvaney, Nano Lett. 4 (2004) 2493.
[155] S. Link, C. Burda, M.B. Mohamed, B. Nikoobakht, M.A. El-Sayed, Phys. Rev. B 61 (2000) 6086.
[156] S. Link, M.A. El-Sayed, Int. Rev. Phys. Chem. 19 (2000) 409.
[157] S. Link, Z.L. Wang, M.A. El-Sayed, J. Phys. Chem. B 104 (2000) 7867.
[158] S. Link, C. Burda, Z.L. Wang, M.A. El-Sayed, J. Chem. Phys. 111 (1999) 1255.
[159] S.L. Logunov, T.S. Ahmadi, M.A. El-Sayed, J.T. Khoury, R.L. Whetten, J. Phys. Chem. B 101 (1997) 3713.
[160] Y. Wang, C. Dellago, J. Phys. Chem. B 107 (2003) 9214.
[161] S. Bharathi, N. Fishelson, O. Lev, Langmuir 15 (1999) 1929.
[162] P.-W. Wu, W. Cheng, I.B. Martini, B. Dunn, B.J. Schwartz, E. Yablonovitch, Adv. Mater. 12 (2000) 1438.
[163] J.F. Hund, M.F. Bertino, G. Zhang, C. Sotiriou-Leventis, N. Leventis, A.T. Tokuhiro, J. Farmer, J. Phys. Chem. B 107 (2003) 465.
[164] W.A. Weyl, Coloured Glasses, Society of Glass Technology, Sheffield, 1951.
[165] S. Braun, S. Rappoport, R. Zusman, D. Avnir, M. Ottolenghi, Mater. Lett. 10 (1990) 1.
[166] M.R. Böhmer, A.R. Balkenende, T.N.M. Bernards, M.P.J. Peeters, M.J. van Bommel, E.P. Boonekamp, M.A. Verheijen, L.H.M. Krings, Z.A.E.P. Vroon, Handbook of Advanced Electronic and Photonic Devices, Academic Press, San Diego, 2001.
[167] S.T. Selvan, T. Hayakawa, M. Nogami, Y. Kobayashi, L.M. Liz-Marzán, Y. Hamanaka, A. Nakamura, J. Phys. Chem. B 106 (2002) 10157.
[168] S. Roorda, T. van Dillen, A. Polman, C. Graf, A. van Blaaderen, B.J. Kooi, Adv. Mater. 16 (2004) 235.
[169] T. van Dillen, A. Polman, W. Fukarek, A. van Blaaderen, Appl. Phys. Lett. 78 (2001) 910.
[170] C.A. Morris, M.L. Anderson, R.M. Stroud, C.I. Merzbacher, D.R. Rolison, Science 284 (1999) 622.
[171] Y. Kobayashi, M.A. Correa-Duarte, L.M. Liz-Marzán, Langmuir 17 (2001) 6375.
[172] B. Rodríguez-González, A. Sánchez-Iglesias, M. Giersig, L.M. Liz-Marzán, Faraday Discuss. 125 (2003) 133.
[173] C. Sanchez, B. Lebeau, F. Chaput, J.-P. Boilot, Adv. Mater. 15 (2003) 1969.
[174] V. de Zea Bermudez, L.D. Carlos, M.C. Duarte, M.M. Silva, C.J.R. Silva, M.J. Smith, M. Assuncao, L. Alcacer, J. Alloys Compd. 275–277 (1998) 21.
[175] V. de Zea Bermudez, L.D. Carlos, L. Alcacer, Chem. Mater. 11 (1999) 569.
[176] B. Sadtler, A. Wei, Chem. Comm. (2002) 1604.
[177] I. Pastoriza-Santos, D. Gomez, J. Pérez-Juste, L.M. Liz-Marzán, P. Mulvaney, Phys. Chem. Chem. Phys. 6 (2004) 5056.
[178] Y. Dirix, C. Bastiaansen, W. Caseri, P. Smith, Adv. Mater. 11 (1999) 223.
[179] B.M.I. van der Zande, L. Pages, R.A.M. Hikmet, A. Van Blaaderen, J. Phys. Chem. B 103 (1999) 5761.
[180] J. Michl, E.W. Thulstrup, J.H. Eggers, J. Phys. Chem. 74 (1970) 3878.
[181] D. Fornasiero, F. Grieser, Chem. Phys. Lett. 139 (1987) 103.
[182] L.A. Bauer, N.S. Birenbaum, G.J. Meyer, J. Mater. Chem. 14 (2004) 517.
[183] M. Wirtz, M. Parker, Y. Kobayashi, C.R. Martin, Chem. Rec. 2 (2002) 259.
[184] M. Wirtz, S. Yu, C.R. Martin, Analyst 127 (2002) 871.
[185] A.J. Haes, D.A. Stuart, S. Nie, R.P. Van Duyne, J. Fluoresc. 14 (2004) 355.
[186] J. Pérez-Juste, B. Rodríguez-González, P. Mulvaney, L.M. Liz-Marzán, Adv. Funct. Mater., 2005, in press.